# COASTAL FLOODING-POTENTIAL PROJECTIONS: 2000–2100

**A White Paper from the California Energy Commission's California Climate Change Center**

Prepared for: California Energy Commission

Prepared by: Scripps Institution of Oceanography


JULY 2012

CEC-500-2012-011

Peter D. Bromirski

Daniel R. Cayan

Nicholas Graham

Mary Tyree

Reinhard E. Flick

Scripps Institution of Oceanography


# ACKNOWLEDGEMENTS

The authors would like to thank the Public Interest Energy Research (PIER) program of the California Energy Commission, who awarded the grant for this research (grant 500-09-038, sub-award POVC02-S02) to the Scripps Institution of Oceanography at the University of California, San Diego. We also thank the Global Climate Model groups who provided the climate model outputs used to generate the wave model and sea level data. Without their efforts and generosity in sharing the data, this work would not have been possible.

In addition, we extend our appreciation to Bill O'Reilly and the Coastal Data Information Program's Monitoring and Prediction program for providing wave transformation matrices; John Helly, at the San Diego Supercomputer Center; and Paul Whittmann, who supplied hindcast wave model data.

Peter D. Bromirski also received support from the National Oceanographic and Atmospheric Administration Climate Change Data and Detection program (grant NA10OAR4310121) and the California Department of Boating and Waterways. In addition, portions of this work were conducted in collaboration with Space and Naval Warfare Systems Command (SPAWAR) Systems Center Pacific (under grant #SI-1703) from the Strategic Environmental Research and Development Program. We acknowledge and thank these organizations.

# ABSTRACT

The change in flooding potential along the California coast over the twenty-first century was estimated from both ocean wave and sea level rise projections produced from global climate model data. Changes in flooding potential were inferred from changes in wave runup (the vertical height reached by wave-driven water levels), which depends on the instantaneous sea level (or still water level), beach slope, and wave height and wave period. The still water level is the superposition of regional (or relative) mean sea level, the tide, and non-tide sea level fluctuations. Non-tide sea level fluctuations include both the steric response associated with El Niño–related variability that can persist up to a year or more, and local storm–forced variability (storm surge). The potential for greatest coastal flooding occurs when extremes in waves and still water level occur nearly simultaneously. Wave activity provides the primary driving force for coastal flooding. Wave model significant wave height (Hs) and non-tide sea level projections were generated for a seven global climate model simulations. Comparison of the Hs and non-tide projections with wave model hindcast Hs and observed non-tide fluctuations suggest that the characteristics and incidence of extreme Hs and non-tide fluctuations will not increase appreciably over the twenty-first century. Thus, because astronomical tide-forcing will not increase, increases in relative mean sea level will largely determine the potential for increased ocean-driven flooding along the California coast. If relative mean sea level along the California coast reaches global mean sea level rise projections associated with climate change, extreme flooding events expected to occur once in about 100 years under stationary relative mean sea levels will occur annually.

**Keywords:** coastal flooding potential, runup, WAVEWATCH III wave model Hs, wave transformation, mean sea level rise projections, non-tide storm surge, joint probability, return period, relative sea level, mean sea level rise projections

Please use the following citation for this paper:

Bromirski, P. D., D. R. Cayan, N. Graham, R. E. Flick, and M. Tyree (Scripps Institution of Oceanography). 2012. ***Coastal Flooding Potential Projections: 2000–2100.*** California Energy Commission. CEC-500-2012-011.

# TABLE OF CONTENTS

**Acknowledgements** ..... **i**

**ABSTRACT** ..... **ii**

**TABLE OF CONTENTS** ..... **iii**

**LIST OF FIGURES** ..... **iv**

**LIST OF TABLES** ..... **vii**

**Section 1: Introduction** ..... **1**

**Section 2: Data and Methods** ..... **3**

2.1 Model Output Sources and Timespans for Data ..... 3

2.2 Mean Sea Level Rise ..... 4

2.3 Non-Tide Fluctuations ..... 5

2.3.1 Historical Variability ..... 5

2.3.2 Projected Variability ..... 5

2.4 Wave Projections ..... 7

2.4.1 Wind Field Adjustments ..... 7

2.5 Wave Variability ..... 8

2.5.1 Dominant Wave Regions over the Eastern North Pacific ..... 8

2.5.2 Offshore California Coastal Wave Projections ..... 10

2.5.3 Nearshore Waves ..... 12

2.6 Extreme Wave Characteristics ..... 14

2.6.1 Extreme Winter Occurrences ..... 14

2.6.2 Frequency of Extreme Winter Events ..... 15

2.6.3 Mean Duration of Extreme Winter Events ..... 16

2.6.4 Azimuths of Extreme Winter Events ..... 17

2.7 Runup ..... 21

2.7.1 Winter Extreme Occurrences ..... 25

2.8 Return Periods from Joint Probability ..... 28

2.8.1 Effect of Beach Slope on Flooding Potential Projections ..... 32

**Section 3: Summary and Conclusions** ..... **33**

3.1 RSL Response to Broad-scale Ocean Circulation Changes ..... 34

**References** ..... **37**

**Glossary** ..... **41**

**Appendix A** ..... **1**

## LIST OF FIGURES

Figure 1. Sea Level Rise Projections. (a) VR global MSL rise projections using the surface air temperature simulations from GCM scenarios given in Table 1. Also included is the altimetry trend estimate of 3 mm/yr (black). (b) Expansion of the time period in (a) of VR estimates approximately common with altimetry. ..... 4

Figure 2. Non-tide Historical and Projected Winter Extremes. (a) Historical non-tide 99th quantile winter (Nov.–Mar.) extremes for which at least 75% of the hourly measurements at Crescent City (CRE), San Francisco (SFO), and La Jolla (SIO) were available. (b)–(d): 99th quantile winter non-tide 2000–2100 projection extremes with mean extreme levels for CCSM3 A1B, A2, and B1 GHG scenarios; CNRM A1 and B1 scenarios; EH4 A2 and B1 scenarios; respectively, at (b) CRE, with mean extreme levels of 41.2, 40.9, 32.1, and 32.2 cm, respectively. CCSM3 trends are not statistically different from zero. CNRM3 downward trends are significant at the 90th percentile level. (c) SFO. Mean extreme levels of 31.8, 31.9, 18.9, and 20.0 cm. CCSM3 trends are not statistically different from zero. CNRM3 downward trends are significant at the 97.5th and 80th percentile levels for A2 and B1 scenarios, respectively. (d) SIO. Mean extreme levels of 14.6, 14.8, 8.6, and 8.7 cm., and the CNRM3 A2 downward trend is significant at the 75th level. The legend in (b) applies to (c) and (d). ..... 6

Figure 3. Spatial Variability of Peak Winter Wave Activity. EOF spatial patterns for winter waves (Nov.–Mar.) over the eastern North Pacific during the 2000–2001 winter determined for WAVWWATCH III wave model Hs forced by the GCM and GHG scenario (Table 1) wind outputs, and by (h) NCEP/NCAR Reanalysis (NRA-1) winds during the 1948–1949 winter. Note that these spatial patterns are just examples of the series of EOFs computed over the winters spanning model time periods 2000–2099 (a), (c), (e), (g) and 2000–2049 (b), (d), (f), with each EOF spatial pattern color-coded from cool-to-warm (weightings low-to-high, respectfully). Also identified are successive winter peaks in the mode 1 EOF (dots), with their associated 98th percentile contours color-coded by year (light-to-dark). The least squares trend line of the longitudinally ordered EOF peaks (magenta line) gives an estimate of the central tendency of peak wave locations. ..... 9

Figure 4. Trends in Latitude and Longitude of Peak Wave Locations. Latitude and longitude of the locations of the EOF mode 1 peaks show the north-south and east-west extents of dominant wave activity by year (winter). Least squares trends (straight lines) are shown for each case.

(a) Hindcast latitude 99th quantile range of the north-south extent (red lines), with the least squares trend (black line) and 5-yr running mean (green line) also shown. (b) Same as (a) except for hindcast longitude, with east-west extent shown instead. (c) GCM projected peak wave latitude locations. (d) GCM projected peak wave longitude locations. Hindcast NRA-1 winter peak locations spanning 1948–2008 (black curves, (c) and (d)) were shifted 52 years. Only the CCSM3 A2 least squares latitude trend is statistically different from zero above the 90th percentile level. Legend color code in (d) also applies trends and to (c). ..... 9

Figure 5. Coastal and Offshore Wave Projection Locations. WaveWatch III hindcast significant wave height (Hs) spatial variation for a major storm event along the California coast during the 1997–1998 El Niño, showing wavefronts propagating southward along the coast. The locations of representative model wave directional spectra projections along the California coast (white circles) are offshore from the primary coastal study sites for which wave transformation matrices are available (yellow circles). Arrows indicate the primary wave spectra locations analyzed. ..... 10

Figure 6. Extreme Offshore Wave Height Variability. Extreme (99th quantile) offshore deep-water Hs projections during winter months for the six GCM wind outputs (Table 1) at deep water WW3 grid locations from north-to-south ([lat,long] deg) designated by (a) Crescent City [42, 234], (b) San Francisco [38, 235.5], (c) Big Sur [36, 237], (d) San Miguel [34, 238.5] (near Pt. Conception), (e) San Diego [33, 240] (southernmost deep water location in Figure 5). The legend in (a) applies to (b)-(e). (f) WW3 forced by NRA-1 winds hindcast 99th quantile winter Hs at the same locations as (a)-(e). All panels have a 7-m Hs range. ..... 11

Figure 7. Extreme Nearshore Wave Height Variability Winter (Nov.–Mar.) extreme (99th quantile) nearshore Hs at California coastal locations close to (from north to south) (a) Crescent City, (b) Crescent City Harbor, (c) Bolinas, (d) Ocean Beach, San Francisco, (e) Santa Cruz, (f) La Jolla Shores, and (g) north of Tijuana near the U.S.-Mexican border. The legend in (f) applies to (a)-(g). All vertical scales span 7 m, except 3.5 m at La Jolla Shores (f). ..... 13

Figure 8. Number of Extreme Winter Occurrences. Projected WW3 Hs occurrences > 5 m during Nov.–Mar. winters forced by GCM winds from the models in Table 1 at offshore locations near (a) Crescent City, (b) San Francisco, (c) San Miguel (see Figure 5 for locations), and (d) hindcast Hs > 5 m at the nearest grid node to the projection locations. Legend in (c) applies to (a) and (b). ..... 15

Figure 9. Frequency of Extreme Winter Events. Number of projected WW3 Hs events during Nov.–Mar. winters where Hs was continuously > 5 m for at least six hours, forced by GCM winds from the models in Table 1 at offshore locations near (a) Crescent City, (b) San Francisco, (c) San Miguel (see Figure 5 for locations), and (d) hindcast Hs > 5 m at the nearest grid node. Legend in (c) applies to (a) and (b). ..... 16

Figure 10. Mean Duration of Extreme Winter Events. Mean duration that Hs was continuously > than 5 m for at least six hours during Nov.–Mar. winters for projected WW3 model waves forced by GCM winds from the models in Table 1 at offshore locations near (a) Crescent City,

(b) San Francisco, (c) San Miguel (see Figure 5 for locations), and (d) hindcast Hs > 5 m at the nearest grid node. Legend in (c) applies to (a) and (b). ..... 17

Figure 11. Winter Medium Azimuth. Median azimuth of all events during Nov.–Mar. winters that Hs was continuously > 5 m for at least 6 hours for projected WW3 model waves forced by GCM winds from the models in Table 1 at offshore locations near (a) Crescent City (CRE), (b) San Francisco (SFO), (c) San Miguel (SML) (see Figure 5 for locations), and (d) hindcast Hs > 5 m. Legend in (a) applies to (b) and (c). ..... 18

Figure 12. North vs. South Azimuths of Extreme Events. The number of extreme events with Hs > 5 m having azimuths of respective peak event Hs > 275o (north, blue) or Hs < 275o (west-southwest, red) near Crescent City (top), San Francisco (middle), and San Miguel (near Pt. Arguello, bottom) for WW3 model NRA-1 hindcast (left), CCSM3 A2 (middle), and EH4 A2 (right) GCM-wind WW3 Hs projections. ..... 19

Figure 13. Extreme Runup Projections – Constant Sea Level. Extreme winter (Nov.–Mar.) 99th quantile runup projection levels using the empirical Stockdon (2006) runup relation for a fixed 2% beach slope. These projections do not include sea level rise, tide, or non-tide projections. ... 23

Figure 14. Extreme Runup Superimposed on Vermeer-Rahmstorf Sea Level Projections. Extreme winter (Nov.–Mar.) 99th quantile runup projection levels using the empirical Stockdon (2006) runup relation for a fixed 2% beach slope. These curves include Vermeer-Rahmstorf (2009) MSL rise, tide, and non-tide projections. ..... 24

Figure 15. Projected Winter Extreme Runup Occurrence. Number of extreme winter (Nov.–Mar.) runup realizations that exceed the 99th quantile runup projection level over the twenty-first century for a fixed 2% beach slope, not including sea level rise. The mean of the 99th quantile level for all seven models at respective locations is annotated. The legend applies to all panels. Note that vertical scales in (a)–(d) differ from (e)–(g). ..... 26

Figure 16. Projected Winter Extreme Runup Occurrence: Including VR SLR Projections. Number of extreme winter (Nov.–Mar.) runup realizations over the 21st century that exceed the no-sea level rise 99th quantile runup projection levels for a fixed 2% beach slope; these estimates include Vermeer-Rahmstorf MSL rise projections. The legend applies to all panels. Note that vertical scales in (a)–(d) differ from (e)–(g). ..... 27

Figure 17. Sea Level Rise Effect on Runup Return Period. Return period curves for the joint probability of runup with tide and non-tide components for no RSL rise (thin solid), the altimetry rise rate of 3 mm/yr (thin dashed), and Vermeer-Rahmstorf (VR) global MSL rise (thick curves). The runup at each location was determined using a 2% beach slope and transformed nearshore wave conditions. Return periods were determined from the joint probability of runup for respective sea level rise projections for the CCSM3 and EH4 A2 GCM realizations, spanning the general range of the A2 GHG scenarios. ..... 30

Figure 18. Return Period Curves. Return period curves for the joint probability of runup and the total instantaneous SWL. The runup at each location was determined using a 2% beach slope. Runup was computed for nearshore wave and sea level conditions forced by waves

superimposed on SWL, incorporating tide+non-tide+Vermeer-Rahmstorf global MSL rise components for the seven GCM realizations (legend; Table 1). These return period panels include the SWL curves in Figure 14. ..... 31

Figure 19. Sensitivity of Return Period to Beach Slope. (a) Joint cumulative probability density functions (CPDF) over 2000–2099 for no sea level rise determined for a spectrum of foreshore beach slopes. All curves were computed for the same nearshore wave, tide, and non-tide sea level conditions forced by CCSM3 A2 GCM wind fields. (b) Return period curves for the CPDFs in (a). ..... 32

Figure 20. Observed Trends. (a) Least squares trends in satellite altimetry sea level height (SLH) across the North Pacific basin over the 1992–2009 time period (after Bromirski et al. 2011). (b) Observed tide-gauge sea level monthly anomalies, with 3-yr running means (red lines) at SFO. Note the near-zero trend along the U.S. West coast in (a) that is reflected in the SFO tide gauge record since about 1980. ..... 34

## LIST OF TABLES

Table 1. Climate Model Simulations. The table shows the time span over which wave model and MSL rise projections were computed for the GHG emission scenario indicated for respective GCMs. ..... 3

Table 2. Wave Model Hindcast vs. Projections: Offshore Wave Statistics 2000–2008. Wave model (WW3) Hs statistics for hindcast (NRA-1) and GCM wind–forced wave model simulations (with peak wave period (Tp)) for offshore locations near (a) Crescent City, (b) San Francisco, and (c) San Miguel. ..... 20

Unless otherwise noted, all tables and figure are provided by the author.

# Section 1: Introduction

This study estimates the change in flooding potential along the California coast over the twenty-first century, of significant societal concern because extensive development along the California coast and enclosed bays has increased the area vulnerable to storm-forced coastal flooding (Heberger et al. 2009).

Regional (or relative) sea level (RSL) along the California coast can differ substantially from global mean sea level (MSL—which herein refers to global levels if not explicitly stated) (Bromirski et al. 2011). Rising RSL increases high-tide water levels and augments extreme storm-forced sea-level fluctuations, allowing more wave energy to reach farther shoreward and thus increasing the potential for coastal flooding.

Coincident occurrence of extremes in short-term sea level fluctuations near high tide results in the greatest coastal impacts, as evidenced by the much greater damage along the central California coast during the strong 1982–1983 El Niño winter than during the 1997–1998 El Niño winter (Storlazzi et al. 2000). Astronomical tide projections, made with good accuracy along the California coast, will not vary significantly over the twenty-first century from historical tide levels, although the tide range at some locations is increasing (Flick et al. 2003).

Thus, the factors that determine whether coastal flooding potential will increase include RSL, non-tide sea level fluctuations (that includes El Niño-related interannual variability, broad-scale decadal changes in ocean circulation, and synoptic storm surge contributions), and ocean wave climate variability. Specifically, flooding is caused by short-term processes superimposed on RSL and results from storm waves impacting the coast during the co-occurrence of high tides and storm surges, with El Niño–related interannual sea level increases augmenting RSL.

Flooding is not driven per se by long-term global MSL rise or rising RSL. But rising RSL increases high tide levels, an important factor in the occurrence of flooding events. Storm waves impacting the coast during low tide generally will not cause coastal flooding. Although the underlying factors that will cause the occurrence and magnitude of flooding events to increase are RSL and waves, especially during strong El Niños (Storlazzi and Griggs 2000), the timing of extreme wave arrivals with respect to high tide is the critical issue (Flick 1998; Storlazzi et al. 2000).

Changes and variability of the coastal flooding potential can be estimated from wave runup above projected RSL. Runup is the vertical distance that storm-forced waves travel up a fixed beach slope above the instantaneous still water level (SWL). The SWL is determined from the superposition of tide and non-tide fluctuations on RSL. In this study, runup variability is used as a proxy for trends and variability of coastal flooding potential.

The study focused on three regions of the California coast that have maintained long duration tide gauge records and that have both sea level and wave variability typical of their respective associated regions:

- The northern coast (NC) (north of Cape Mendocino) at Crescent City (CRE)
- The central coast (CC) (from Cape Mendocino to Point Conception) at San Francisco (SFO)
- The southern coast (SC) (south of Point Conception) at La Jolla (SIO)

Specifically, flooding potential projections incorporated the following components:

- Estimated changes and variability of coastal flooding potential over 2000–2099 using sea level and ocean wave projections derived from global climate model (GCM) output fields
- Examined outputs from seven GCM simulations, spanning either 2000–2049 or 2000–2099, from three climate centers for four different greenhouse gas (GHG) emission scenarios (see Table 1)
- Obtained global MSL estimates using GCM surface air temperatures following the methodology of Vermeer and Rahmstorf (VR) (2009)
- Projected non-tide sea level fluctuations using GCM wind, sea level pressure, and NINO3.4 sea surface temperature data following Cayan et al. (2008)
- Computed deep-water wave directional spectra at selected offshore locations using the WAVEWATCH III (WW3) wave model (Tolman 1999) forced by GCM winds
- Transformed offshore waves to nearshore locations using California Data Information Program (CDIP) monitoring and prediction (MOP) system wave transformation matrices, and then used the sea level and nearshore wave projections as input to the empirical runup formulation presented by Stockdon et al. (2006)
- Applied probability density functions of instantaneous sea level and runup to determine the joint probability of changes in the return periods of these parameters for the cases of stationary RSL, the current global MSL rise rate of about 3.1 +/- 0.7 mm/yr (Timmermann et al. 2010), and the VR GCM surface air temperature-based MSL rise projections

# Section 2: Data and Methods

## 2.1 Model Output Sources and Timespans for Data

Estimates of changes and variability of coastal flooding potential over 50–100 year epochs require both wave and sea level rise projections using outputs from the same GCM simulations. The WAVEWATCH III wave model (WW3) (Tolman 1999) requires GCM wind estimates every 6 hours—a requirement that restricts the number of GCMs available because not all climate centers have saved wind estimates at this relatively high sample rate. Seven GCM simulations were obtained with six-hour wind estimates to generate wave model projections. These seven GCM simulations also have surface air temperature, sea level pressure (SLP), and NINO3.4 SST data available to estimate global MSL rise and short-term sea level fluctuations.

Model outputs were obtained from the following GCMs (see Section 2.4 for additional GCM description):

- National Center for Atmospheric Research (NCAR) Community Climate System Model (CCSM3)
- Centre National de Recherches Meteorologiques (CNRM) CM3 model
- Max Planck Institute for Meteorology (MPI) EH4 model

These ouptuts span at least 100 years for the higher GHG emissions scenarios (A2 and A1B) assessed by the Intergovernmental Panel on Climate Change (IPCC), and at least 50 years for the lower GHG emission scenarios (B1 and B2) (IPCC 2007). Table 1 summarizes the GCM data obtained for each GHG emission scenario.

**Table 1. Climate Model Simulations. The table shows the time span over which wave model and MSL rise projections were computed for the GHG emission scenario indicated for respective GCMs.**

| GHG Scenario | GCM Origin | Years |
|---|---|---|
| A1B | CCSM3 | 2000–2099 |
| A2 | CCSM3 | 2000–2099 |
| A2 | CNRM | 2000–2099 |
| A2 | EH4 | 1990–2099 |
| B1 | CCSM3 | 2000–2049 |
| B1 | CNRM | 2000–2049 |
| B2 | EH4 | 1990–2049 |

## 2.2 Mean Sea Level Rise

Global MSL rise projections were estimated from GCM annual surface air temperature projections using the VR methodology (Vermeer and Rahmstorf 2009). The IPCC (IPCC 2007) projected a global sea level rise of 18 to 59 centimeters from 1990 to the 2090s, plus an unspecified amount of rise that could result from ice losses in the large ice sheets covering Greenland and Antarctica. The current global satellite altimetry trend (Aviso 2010) spanning 1992–2009 is about 3.1 +/- 0.7 mm/yr (Timmermann et al. 2010), giving an MSL rise at 2100 of about half the IPCC upper bound (Bindoff and coauthors 2007).

The VR MSL rise projections derived from GCM surface air temperature data have similar characteristics (Figure 1a; Cayan et al. 2012). That is, the projections show an approximately parabolic increase over the twenty-first century that accelerates towards the end of the century. Figure 1b, which compares these projections with the global altimetry trend estimate over 2000–2012, indicates that the VR methodology generally overestimates MSL rise over the satellite epoch ,with the projections using EH4 data most closely matching the altimetry trend at the beginning of the century. This difference between VR MSL projections and altimetry is an issue that will be resolved as the altimetry record lengthens. However, the current altimetry and tide gauges trends suggest that the VR estimates are likely upper bounds for RSL rise along the California coast.

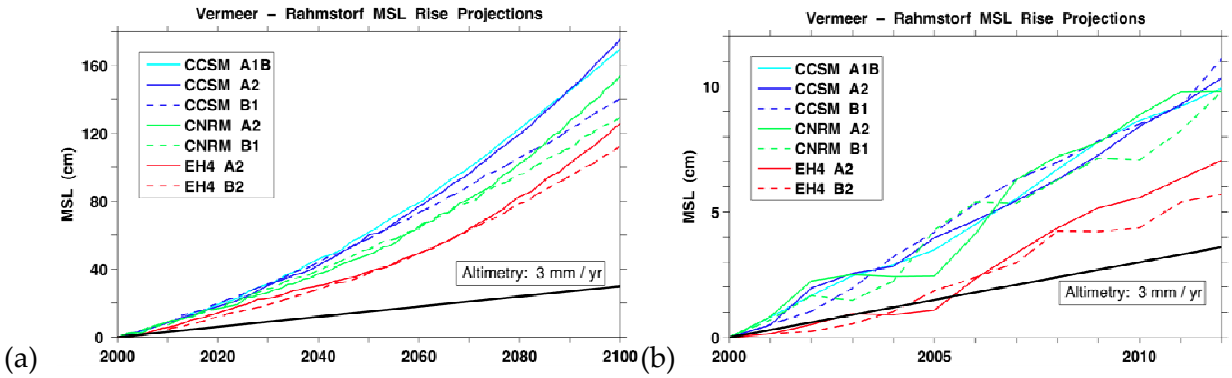


**Figure 1. Sea Level Rise Projections. (a) VR global MSL rise projections using the surface air temperature simulations from GCM scenarios given in Table 1. Also included is the altimetry trend estimate of 3 mm/yr (black). (b) Expansion of the time period in (a) of VR estimates approximately common with altimetry.**

## 2.3 Non-Tide Fluctuations

Sea level fluctuations (excluding wave activity) superimposed on the tide result from a combination of the following:

- Low SLP causing the inverse barometer effect (sea level is raised about 1 cm per 1 mm drop in SLP)
- Coastal winds
- El Niño–associated increases (Chelton and Davis 1982; Bromirski et al. 2003; Storlazzi and Griggs 2000).

During great El Niños, such as the 1982–83 and 1997–98 events, sea level along the California coast can be elevated by 15–20 cm for more than 6 months, generally spanning the winter storm season. This interannual El Niño coastal effect results from a combination of high amplitude, poleward-propagating, coastally-trapped waves and thermal expansion associated with warmer water off the coast. The resulting several-month increase in California coastal sea levels can be compared to those observed during the entire twentieth century. Prior to the 1982–83 event, the 1940–41 and 1915–16 El Niño events stand out, suggesting that intense El Niños may be occurring more frequently.

### 2.3.1 Historical Variability

Coastal flooding potential is enhanced during non-tide extremes, which occur during extreme coastal storm events that generally also produce high rainfall and river flows (Bromirski and Flick 2008). In general, historical tide gauge measurements along the California coast show that trends in winter (November–March) 99th quantile non-tide extremes are not significantly different from zero at the 99th percentile level (Figure 2a).

These trends are determined throughout this paper using a 2-sided T-test linear regression hypothesis test, assuming the underlying distribution is approximately normally distributed (Hines and Montgomery 1980). This method is in contrast to estimates of increased storminess derived from buoy significant wave height (Hs) data (Ruggiero et al. 2010). Recently, however, Gemmrich et al. (2011) showed that upward trends in storminess derived from buoy Hs data generally are biased due to changes in processing methodology and buoy type and that buoy-derived upward trends in eastern North Pacific storminess data are generally either overestimated or not statistically significant, consistent with non-tide trends shown here.

However, the mean of the non-tide 99th quantile increases significantly from south to north: 13.5 cm at SIO, 26.6 cm at SFO, and 38.7 cm at CRE, consistent with Bromirski and Flick (2003). This northward increase is associated with the location of the dominant storm track, which affects the portion of the coastline where the strongest storm intensity occurs, i.e., the near-coastal SLP minimum.

### 2.3.2 Projected Variability

Non-tide projections at CRE, SFO, and SIO (Figure 2b–d), determined using the methodology of Cayan et al. (2008), show a similar pattern of northward increasing non-tide levels, suggesting that storm tracks may not change significantly. In general, trends in the 99th quantile extremes

are generally flat, although some have a downward bias that is consistent with a northward shift in storm track going forward. Individually, the GCMs generally produce about the same projections for both the high and low GHG scenarios examined, with the exception of the highly significant downward trend for the CCSM3 A2 extremes at SIO.

The overlapping period of the projections with the observations suggests that the CCSM3 extreme non-tide projections are near or somewhat higher than historical extremes and that the CNRM and EH4 estimates generally lower. At CRE, only the CNRM A2 and B1 trends are statistically significant at the 95th percentile level. At SFO, only the CNRM A2 and B1 trends are statistically significant at the 95th and 90th levels, respectively. The extreme non-tide projections suggest that the non-tide contributions to the total water level during storm events, i.e., storm surge, will not change appreciably over the twenty-first century, and thus will not contribute to an increased flooding potential risk along the California coast.

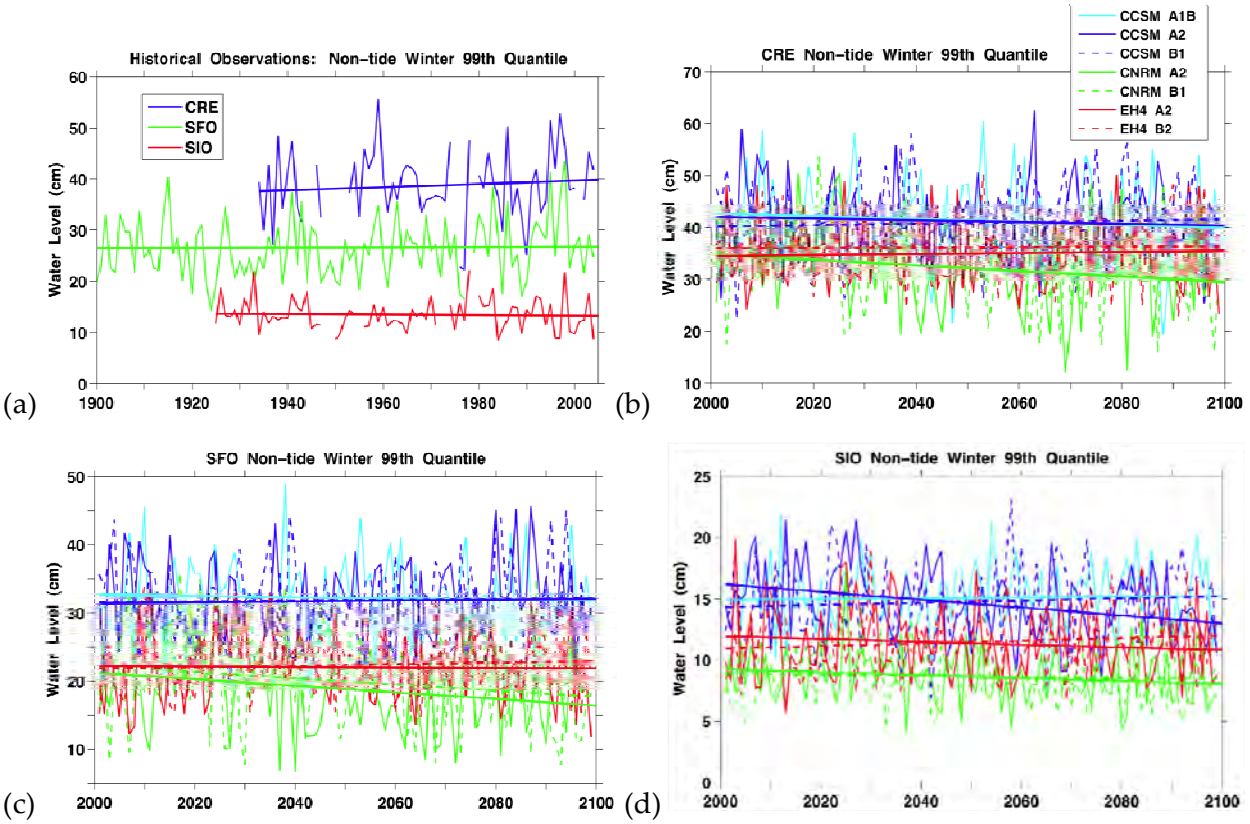


**Figure 2. Non-tide Historical and Projected Winter Extremes. (a) Historical non-tide 99th quantile winter (Nov.–Mar.) extremes for which at least 75% of the hourly measurements at Crescent City (CRE), San Francisco (SFO), and La Jolla (SIO) were available. (b)–(d): 99th quantile winter non-tide 2000–2100 projection extremes with mean extreme levels for CCSM3 A1B, A2, and B1 GHG scenarios; CNRM A1 and B1 scenarios; EH4 A2 and B1 scenarios; respectively, at (b) CRE, with mean extreme levels of 41.2, 40.9, 32.1, and 32.2 cm, respectively. CCSM3 trends are not statistically different from zero. CNRM3 downward trends are significant at the 90th percentile level. (c) SFO. Mean extreme levels of 31.8, 31.9, 18.9, and 20.0 cm. CCSM3 trends are not statistically different from zero. CNRM3 downward trends are significant at the 97.5th and 80th percentile levels for A2 and B1 scenarios, respectively. (d) SIO. Mean extreme levels of 14.6, 14.8, 8.6, and 8.7 cm., and the CNRM3 A2 downward trend is significant at the 75th level. The legend in (b) applies to (c) and (d).**

## 2.4 Wave Projections

The WW3 model domain for the GCM projections covered the region 20°N to 60°N (Aleutian Islands/Alaskan coast) and 120°E (Asian coast) to 240°E (North American coast). The WW3 model provides spatial resolution of 1.0° x 1.5° latitude/longitude, 5° directional resolution (72 bins), and 20 logarithmically spaced frequency bins (period range ~4.4 to 27.2 s). Winds from three GCMs (Table 1) were used:

- CCSM - NCAR CCSM3 (version 3.0 beta19; IPCC Fourth Assessment) having spatial resolution of ~1.4° latitude-longitude with near-surface winds from lowest model sigma level (~62 m elevation) (e.g., Kiehl et al. 2006; Collins et al. 2006a,b)
- CNRM - CM3 coupled model (IPCC Fourth Assessment) having spatial resolution of ~1.9° latitude and ~2.8° longitude with near-surface winds nominally at 10 m elevation (Kvamstø et al. 2008).
- EH4 - MPI ECHAM4 atmospheric model coupled to an OPYC ocean model having spatial resolution of ~2.8° latitude and longitude. (e.g., Legutke and Voss 1999; Stendel and Roekner 1998).

### 2.4.1 Wind Field Adjustments

Prior to performing the final simulations with WW3, the climate model (CCSM, CNRM, EH4) wind fields were adjusted to bring their modern (late twentieth–early twenty-first century) winter (November–March) wave climatologies into approximate agreement with those from WW3 when driven with National Oceanic and Atmospheric Administration (NOAA) National Centers for Environmental Prediction (NCEP) reanalysis project (NCEP-RA1; Kalnay et al. 1996) (e.g., Graham 2005; Caires et al. 2004.

The NCEP-RA1 winds have a spatial resolution of about 1.9° degrees latitude/longitude and near-surface winds nominally at 10-meter elevation. NCEP-RA1 data used for GCM wind calibration cover 1970–1999. The adjustments for each of the models account for differences in the nominal elevation of the near-surface winds, model boundary layer formulations (leading to disparities in 10 m winds), and (to some extent) wind and cyclone climatologies. The adjustments, focused primarily on the central and eastern North Pacific, were made using the boundary layer wind profile algorithm described by Liu et al. (1979). This algorithm conceptually adjusts the winds from a nominal "observation height" to a desired "reference height" in accordance with the wind speed- and stability-dependent vertical wind profile. No changes were made to wind direction, with neutral stability assumed. Changes in reference height were applied uniformly in space.

For each climate model, the adjustment procedure was done in two steps:

- The climate model and NCEP-RA1 winter wind fields were compared (focusing on the 90th and 95th wind speed quantiles) to obtain a first estimate of the reference height adjustment required.

- After making this initial adjustment, the wave model was run iteratively for a series of 20–30 year simulations, comparing the wave model output to the NCEP-RA1-driven WW3 results after each simulation. These comparisons focused on the more extreme 90th to 99th percentile $H_S$ in the central and eastern North Pacific.

When satisfactory agreement was obtained, the final simulation for that model was performed using this "best" reference level adjustment. Over the 10–20 $ms^{-1}$ range, the final adjustments resulted in 21–24 percent wind speed reductions for the CCSM data, 10 percent increases for CNRM, and 5 percent decreases for EH4. The level of agreement in $H_S$ obtained is illustrated in Figure A1, (see Appendix A) which shows comparisons of the frequency distributions of winter (November–March) $H_S$ from the climate model simulations for 1991–2020, and those from the NCEP-RA1 results for 1970–99, for four locations in the North Pacific.

## 2.5 Wave Variability

Waves provide nearly all the energy that drives physical processes along the California coast, and the occurrence of high waves relative to tidal extremes produces coastal flooding as well as beach and sea cliff erosion. Surface gravity waves are generated by wind blowing over the ocean and are characterized by their height, period, and direction of propagation. These wave parameters are jointly characterized by the wave "frequency-directional spectrum," which is the distribution of wave energy (proportional to height squared) as a function of wave frequency (the inverse of period) and direction. The wave spectrum of deep-water ocean waves depends in turn on the strength of the generating wind field (wind speed), the size of the area the wind is blowing over (fetch), and how long sustained wind speeds persist (duration). Big storms with persistent strong winds that blow over large ocean areas for several days generate high waves with long periods (i.e., low frequencies).

### 2.5.1 Dominant Wave Regions over the Eastern North Pacific

Identification of a systematic change in the location of the dominant winter wave generation region is important to estimate changes in flooding potential. The proximity of the wave generation region to the California coast affects both wave amplitude and incident wave direction. The variability of the dominant wave generation region during winter (November–March) over the eastern North Pacific was estimated by computing successive winter empirical orthogonal functions (EOFs) of WW3-generated Hs wavefields for the model winds studied (Table 1) and also for WW3 hindcast wave model Hs forced by NCEP NCAR Reanalysis winds (NRA-1). Changes in the location of the peak of the Hs mode 1 EOF gives an estimate of the range of variability of the location of the dominant winter wave heights.

#### *2.5.1.1 Broad-Scale Patterns*

Comparing the NRA-1 hindcast mode 1 peak winter wave location estimates (Figure 3h) with those forced by CCSM3 and CNRM winds (Figures 3a–d) suggests that peak wave activity will move north and closer to the Pacific coast of North America during some twenty-first century winters. Hindcast peak wave locations suggest that the dominant centers of wave activity have been more southerly over the last two decades compared to earlier activity. The hindcast EOF peaks also suggest that the dominant wave activity was generally somewhat farther from the

coast. The pattern of peak locations produced by EH4 A2 and B2 winds (Figures 3e,f) appears to more closely match NRA-1 hindcast winters. The central tendency of peak wave activity (Figure 3, magenta lines) show a northeastward trend for the GCM projections, typically more pronounced than for NRA-1 hindcast winters.

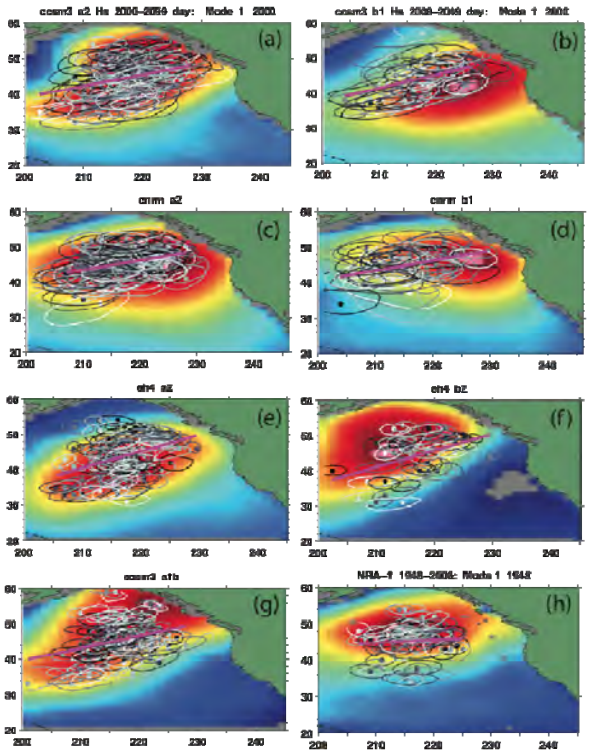


**Figure 3. Spatial Variability of Peak Winter Wave Activity. EOF spatial patterns for winter waves (Nov.–Mar.) over the eastern North Pacific during the 2000–2001 winter determined for WAVWWATCH III wave model Hs forced by the GCM and GHG scenario (Table 1) wind outputs, and by (h) NCEP/NCAR Reanalysis (NRA-1) winds during the 1948–1949 winter. Note that these spatial patterns are just examples of the series of EOFs computed over the winters spanning model time periods 2000–2099 (a), (c), (e), (g) and 2000–2049 (b), (d), (f), with each EOF spatial pattern color-coded from cool-to-warm (weightings low-to-high, respectfully). Also identified are successive winter peaks in the mode 1 EOF (dots), with their associated 98th percentile contours color-coded by year (light-to-dark). The least squares trend line of the longitudinally ordered EOF peaks (magenta line) gives an estimate of the central tendency of peak wave locations.**

### *2.5.1.2 Variability of Dominant Winter Wave Locations*

Substantial north-south and east-west interannual variability of the location of peak winter Hs is observed (Figure 4). More southerly and easterly centers of peak wave activity would have higher flooding risk for the California coast. Trend lines, which give estimates of the variability of mean latitude and longitude peak wave activity over time, suggest that greater variability was observed over the historical 1948–2008 epoch than is projected over the twenty-first century. Model projections over the twenty-first century generally suggest a tendency for peak Hs shifting to more northerly latitudes (Figures 4c,d; 3a–d,g) and closer to the coast. The model projection longitude trends (Figure 4d) suggest that the average distance of peak Hs from the coast will not change appreciably from current locations over the twenty-first century.

The bi-modal distribution of hindcast winter peak locations (Figure 3h) results in a decreasing latitude trend over the latter half of the twentieth century (Figure 4a, black line). However, hindcast winter five-year running means (Figures 4a,b; green curves) show a general tendency for a northeastward shift in the dominant centers of wave activity since about 1995, in general agreement with the projections. The general tendency for more northward centers of peak wave activity may be related to variability of broad-scale atmospheric patterns associated with the Pacific decadal oscillation (PDO) and regional wind patterns (Miller et al. 1994; Bromirski et al. 2011). More northerly centers of peak wave activity would be expected to result in a reduction in extreme waves along the California coast, particularly south of Cape Mendocino, with an associated reduced risk for flooding events.

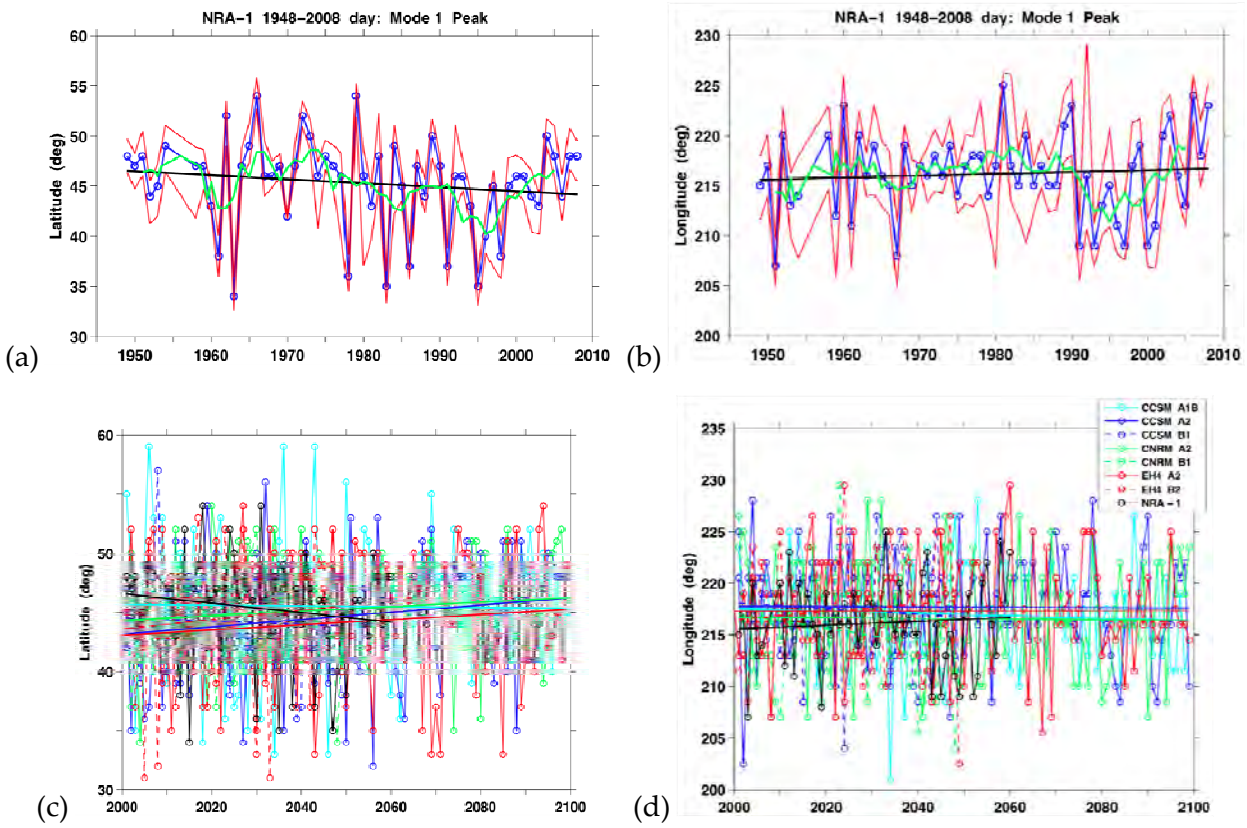


**Figure 4. Trends in Latitude and Longitude of Peak Wave Locations. Latitude and longitude of the locations of the EOF mode 1 peaks show the north-south and east-west extents of dominant wave activity by year (winter). Least squares trends (straight lines) are shown for each case. (a) Hindcast latitude 99th quantile range of the north-south extent (red lines), with the least squares trend (black line) and 5-yr running mean (green line) also shown. (b) Same as (a) except for hindcast longitude, with east-west extent shown instead. (c) GCM projected peak wave latitude locations. (d) GCM projected peak wave longitude locations. Hindcast NRA-1 winter peak locations spanning 1948–2008 (black curves, (c) and (d)) were shifted 52 years. Only the CCSM3 A2 least squares latitude trend is statistically different from zero above the 90th percentile level. Legend color code in (d) also applies trends and to (c).**

### 2.5.2 Offshore California Coastal Wave Projections

The wave climate along the California coast was characterized from WW3 wave model projections forced by six-hour wind outputs from three GCMs (Table 1). Because wave conditions along the California coast are highly coherent over relatively large spatial scales (Bromirski et al. 1999; Bromirski et al. 2005), wave variability is sufficiently characterized by wave estimates at five deep-water locations (Figure 5, more oceanward white circles) that represent the three wave regimes along the California coast (NC, CC, and SC), delineated in Section 1.0.

To provide a reference for the WW3 wave model projections along the California coast, hindcast Hs forced by NRA-1 winds were compared with the wave model projections at nearly the same locations. Mean Hs projections offshore Crescent City, San Francisco, and near Point Arguello at San Miguel (arrows in Figure 5) are significantly higher than the NRA-1 hindcast Hs for most of the GCM model wind-forced Hs, except the EH4 A2 and B2 model scenarios (Figure 6).

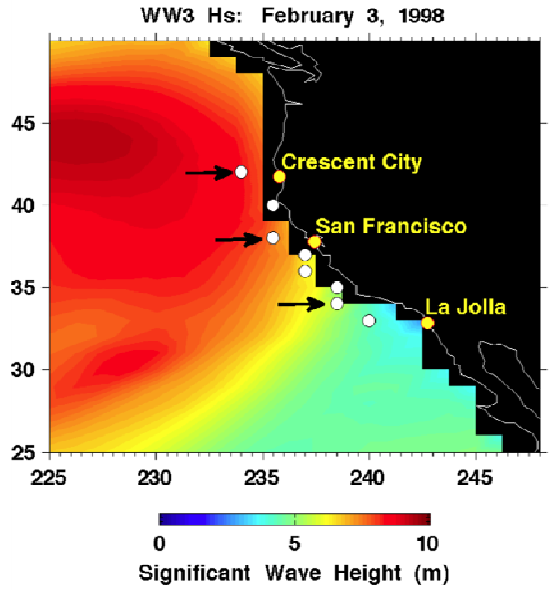


**Figure 5. Coastal and Offshore Wave Projection Locations. WaveWatch III hindcast significant wave height (Hs) spatial variation for a major storm event along the California coast during the 1997–1998 El Niño, showing wavefronts propagating southward along the coast. The locations of representative model wave directional spectra projections along the California coast (white circles) are offshore from the primary coastal study sites for which wave transformation matrices are available (yellow circles). Arrows indicate the primary wave spectra locations analyzed.**

Extreme wave variability projections along the California coast can be characterized by changes in the 99th quantile Hs during winter months (Figure 6). The GCM wind-forced waves in general show extreme Hs decreasing in amplitude from north-to-south, consistent with projected spatial patterns and locations of peak wave activity (Figures 3 and 4), and with buoy observations (Bromirski et al. 1999; Bromirski et al. 2005). The CCSM3 and CNRM simulations generally produced higher amplitude waves than the EH4 model. Only the CCSM3 A2

downward trend is statistically different from zero at the 95th percentile level and at all locations.

Hindcast WW3 99th quantile winter Hs extreme amplitude estimates (Figure 6f) generally compare favorably with the projections. Hindcast upward trends are statistically different from zero at the 90th percentile level at all locations except northernmost CRE, where the CCSM3 and CNRM models project significantly higher winter extremes.

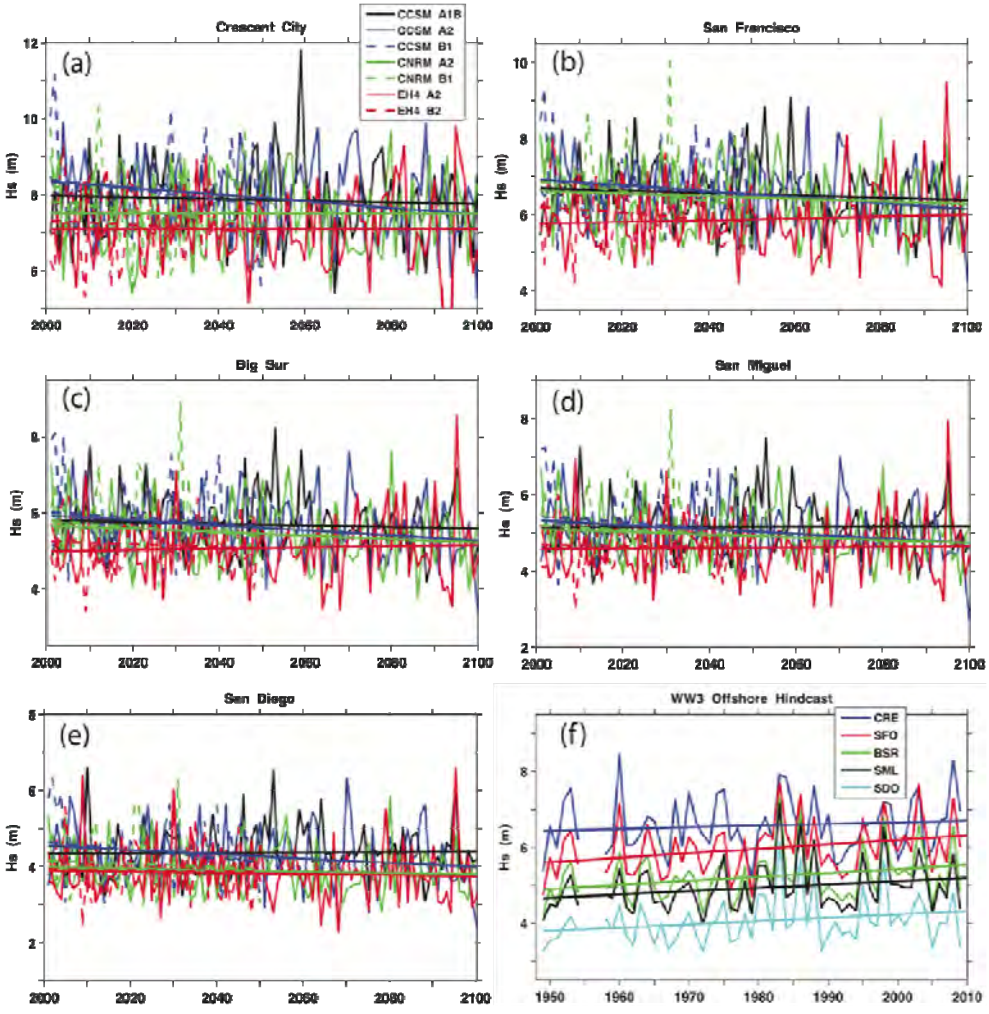


**Figure 6. Extreme Offshore Wave Height Variability. Extreme (99th quantile) offshore deep-water Hs projections during winter months for the six GCM wind outputs (Table 1) at deep water WW3 grid locations from north-to-south ([lat,long] deg) designated by (a) Crescent City [42, 234], (b) San Francisco [38, 235.5], (c) Big Sur [36, 237], (d) San Miguel [34, 238.5] (near Pt. Conception), (e) San Diego [33, 240] (southernmost deep water location in Figure 5). The legend in (a) applies to (b)-(e). (f) WW3 forced by NRA-1 winds hindcast 99th quantile winter Hs at the same locations as (a)-(e). All panels have a 7-m Hs range.**

### 2.5.3 Nearshore Waves

The dominant physics affecting shallow water waves along the California coast are interactions with ocean bottom bathymetry causing wave refraction and shoaling, which are complicated by island and headland sheltering. Particularly in the Southern California Bight, islands and coastline configuration can shield particular coastal stretches. Depending on wave azimuth, wave period, and local bathymetry, focusing of wave energy can strongly affect longshore sediment transport and coastal erosion potential (O'Reilly and Guza 1991; Graham 2005; Adams et al. 2011). The CDIP coastal wave modeling system (MOP) (O'Reilly and Guza 1991; 1993) accounts for wave refraction, shoaling, and local bathymetry effects on nearshore wave amplitudes. The CDIP deep-to-shallow water wave transformation model has been optimized to minimize wave direction errors in very shallow water prior to wave breaking. Shallow water directional wave information is critical to predict nearshore wave characteristics essential for runup estimation.

MOP wave transformation matrices were obtained for representative low and high wave-energy locations in the California north (NC), central (CC), and southern (SC) coastal regions, near coastal stations where long tide gauge records were available to calibrate the non-tide projections. Extreme nearshore wave variability (Figure 7) generally tracks the respective offshore wave variability shown in Figure 6. Differences between offshore and nearshore waves are greatest in the SC region (compare Figure 6d,e with Figure 7f,g) as a result of island shadowing and more complicated bathymetry south of Pt. Arguello. Differences between model simulations are also greatest in the SC region. In particular, CNRM A2 nearshore Hs at the SC locations (Figures 7f,g) generally decreases more than Hs from the EH4 simulations, emphasizing the importance of robust directional wave transformation matrices for particular coastal locations under differing wave directions. This difference also emphasizes the importance of wave azimuth in the SC region (O'Reilly and Guza 1991; Graham 2005; Adams et al. 2011). Note that mean nearshore Hs near the U.S. border (Figure 7g, represented by the trend line) is about twice that at La Jolla (Figure 7f), a well-sheltered location. Nearshore trends generally follow respective offshore trends. As for the offshore waves, only the CCSM3 A2 trend is statistically different from zero, at the 90th percentile level at all locations.

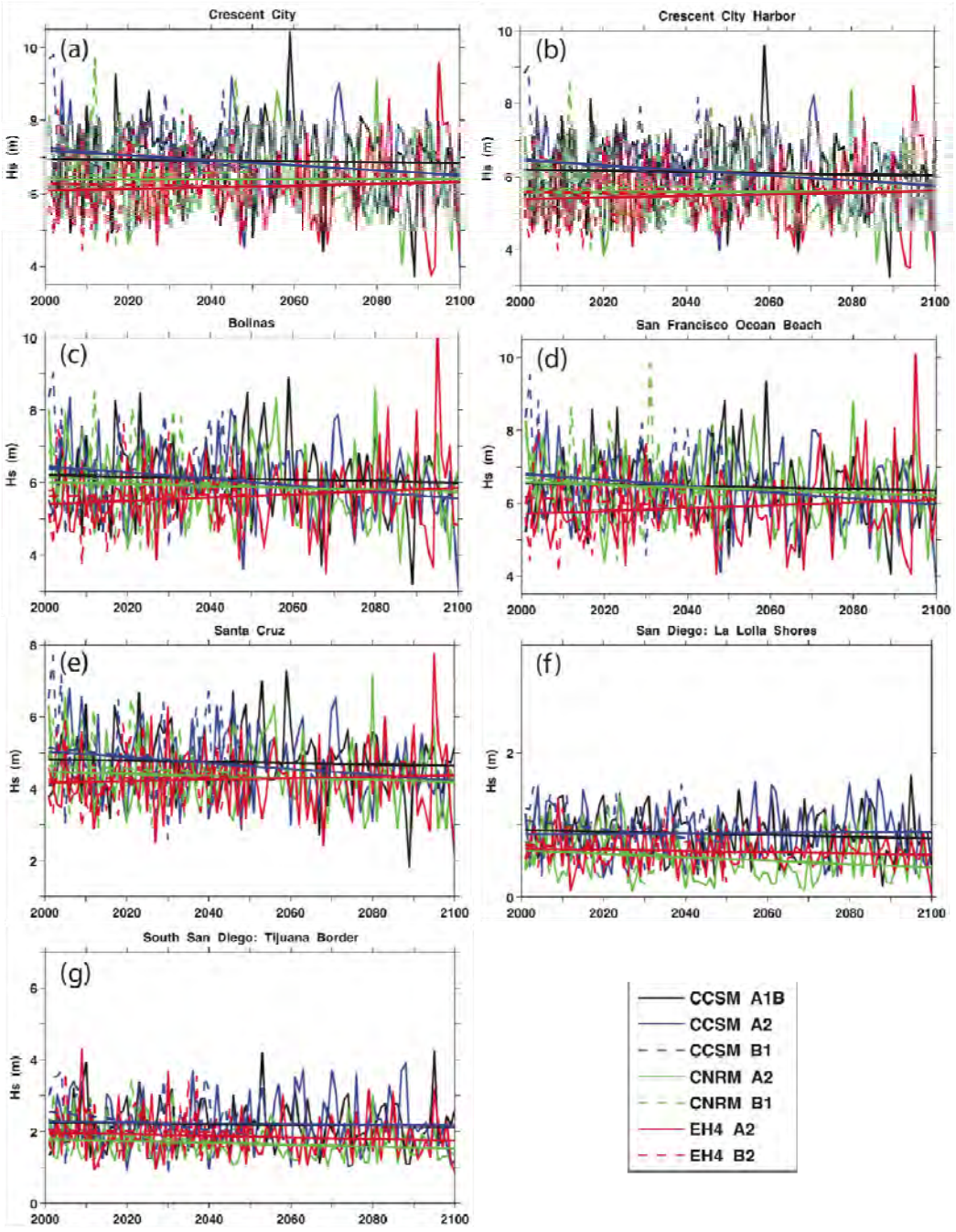


**Figure 7. Extreme Nearshore Wave Height Variability Winter (Nov.–Mar.) extreme (99th quantile) nearshore Hs at California coastal locations close to (from north to south) (a) Crescent City, (b) Crescent City Harbor, (c) Bolinas, (d) Ocean Beach, San Francisco, (e) Santa Cruz, (f) La Jolla Shores, and (g) north of Tijuana near the U.S.-Mexican border. The legend in (f) applies to (a)-(g). All vertical scales span 7 m, except 3.5 m at La Jolla Shores (f).**

## 2.6 Extreme Wave Characteristics

Because astronomical high tide levels will not change significantly by 2100, the key factors that affect changes in runup heights and associated flooding potential are coastal RSL and waves. As suggested by offshore and nearshore winter extreme Hs (Figures 6 and 7), winter wave extremes should be similar to historical levels. However, critical to coastal impacts and the potential for coastal flooding are the frequency and characteristics of extreme wave events, including the peak amplitude, duration, and azimuth of the most extreme waves, as well as the occurrence of these waves with respect to high tide. In general, the Hs amplitudes for the most extreme events in Figures 6 and 7 are higher in the north than in the south, showing a general decrease that is consistent with a more northerly wave generation region, resulting in decreasing Hs as the swell propagates southward along the coast, as demonstrated in Figure 5 for an extreme wave event.

In addition to the magnitude of extreme winter Hs, an important consideration to estimate whether flooding incidence will become more frequent over the twenty-first century is whether the number of extreme wave occurrences during each winter (November–March) will increase. This study characterized extreme Hs frequency along the California coast by examining WW3-generated model output using a 5 m threshold. The winter extreme Hs characteristics examined include the following:

- The number of occurrences above threshold
- The number of extreme events each winter, where Hs is continuously > 5 m for at least six hours
- The mean duration of all extreme Hs events in each winter
- The median azimuth of extreme Hs events

Because ocean swell is well-correlated over large spatial regions along the California coast (Bromirski et al. 1999), three locations should be adequate to characterize the spatial variability: in the north near Crescent City (CRE), near San Francisco (SFO), and in the south at near San Miguel (SML) (arrows, N-S, in Figure 5). The trends give estimates of the change in the mean of that wave characteristic over time.

### 2.6.1 Extreme Winter Occurrences

Substantial interannual variability for each WW3 projection and between the model-generated extreme waves is realized (Figure 8). The EH4 winds generally produce the lowest number of extreme waves, typically about 50 percent and 25 percent less than the CCSM3 and CNRM models, respectively. Only the EH4 B2 model shows an increasing number of extreme wave occurrences, while the other projections show downward trends, with only the CCSM3 A1b and A2 trends statistically significant above the 90th percentile level at CRE and SFO. The EH4 projections most closely match recent hindcast Hs extreme occurrences, suggesting that both the CCSM3 and CNRM GCM winds are biased high. The upward trends for the hindcast extreme occurrences at CRE and SFO (Figure 8d) are statistically significant at the 90th and 97.5th significance levels, respectively. Although the CCSM3 and CNRM GCM calibrated winds may be biased high, resulting in a corresponding high bias in WW3 model Hs, the general

consistency of the downward trends across these models suggests that the upward trends exhibited in hindcast Hs extreme occurrence will not persist.

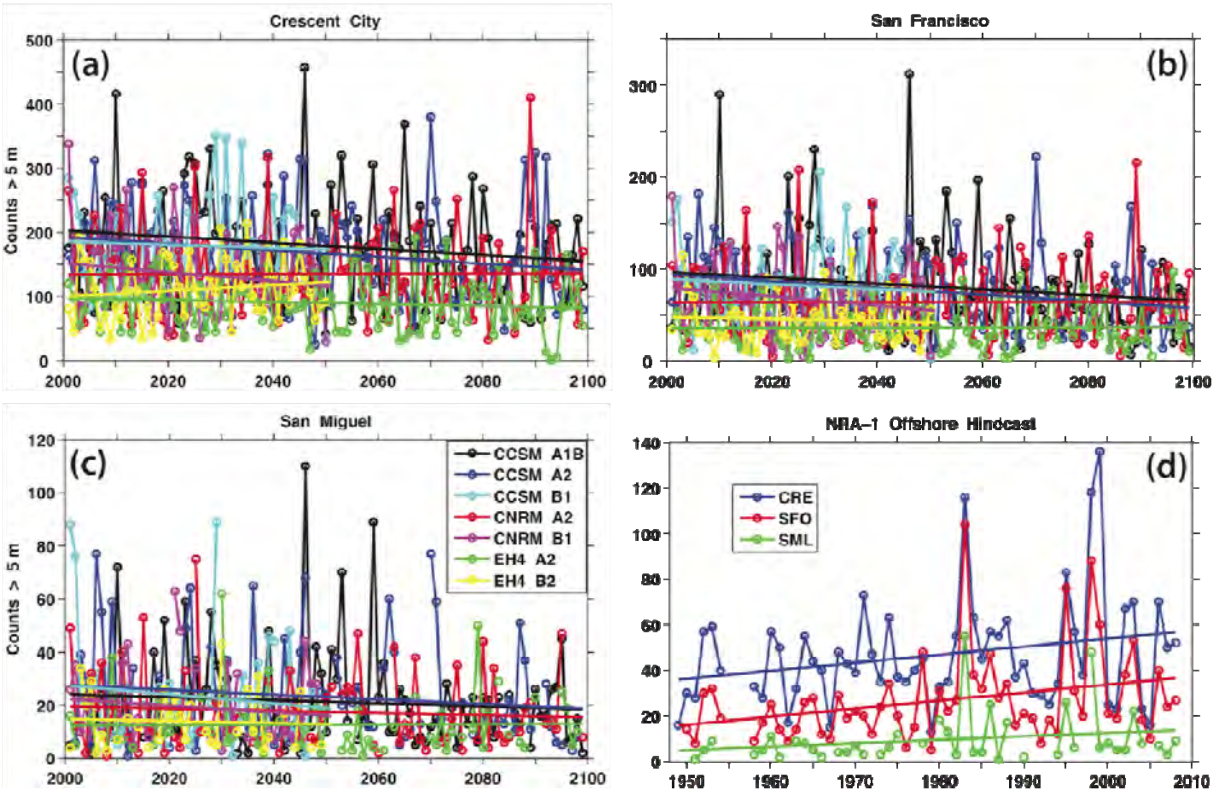


**Figure 8. Number of Extreme Winter Occurrences. Projected WW3 Hs occurrences > 5 m during Nov.–Mar. winters forced by GCM winds from the models in Table 1 at offshore locations near (a) Crescent City, (b) San Francisco, (c) San Miguel (see Figure 5 for locations), and (d) hindcast Hs > 5 m at the nearest grid node to the projection locations. Legend in (c) applies to (a) and (b).**

### 2.6.2 Frequency of Extreme Winter Events

Extreme events, with Hs continuously >5 m for at least six hours, were identified objectively (Figure 9). There is the possibility that an individual event having multiple phases (i.e., where Hs drops below 5 m for one or two observations) could be counted as more than one event. However, because this situation would likely occur at about a similar incidence rate at each location, projections of extreme event incidence should be equally biased and comparisons between the models should be valid. Extreme events do not occur each winter, which is especially true at the southernmost (San Miguel, SML; Figure 5, southernmost arrow) location examined.

Substantial interannual variability is observed for both projections and hindcast Hs. However, the projected number of extreme events has a decreasing tendency, particularly at southernmost SML. This pattern is consistent with more northerly dominant wave generation regions in the

future. Only the hindcast downward trend at SFO is statistically different from zero, above the 97.5th percentile level. The CCSM3 A2 projection trends at SFO and SML are also significant, above the 95th level.

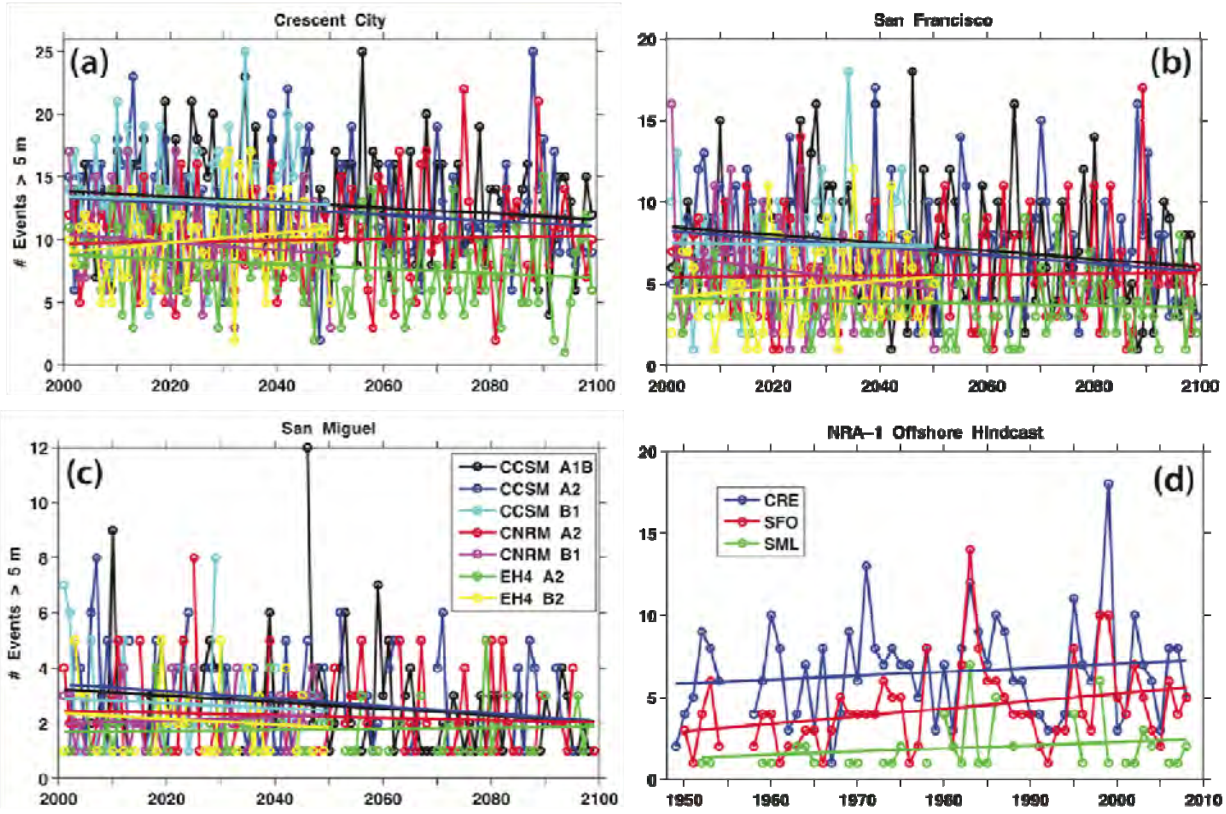


**Figure 9. Frequency of Extreme Winter Events. Number of projected WW3 Hs events during Nov.–Mar. winters where Hs was continuously > 5 m for at least six hours, forced by GCM winds from the models in Table 1 at offshore locations near (a) Crescent City, (b) San Francisco, (c) San Miguel (see Figure 5 for locations), and (d) hindcast Hs > 5 m at the nearest grid node. Legend in (c) applies to (a) and (b).**

### 2.6.3 Mean Duration of Extreme Winter Events

As the duration of extreme events increases, the likelihood of extreme waves during high tide also increases. In general, the WW3 projections suggest that the duration of extreme events will not increase, with a slight downward bias in their duration over the twenty-first century (Figure 10). The pattern of interannual variability in mean duration, in both WW3 projections and hindcast Hs data, indicates that some winters will experience mean event duration about double the trend-line (Figure 10d). Trends in mean duration of hindcast extreme events (Figure 10d) are not statistically significant. Only the CCSM3 A2 at CRE and SFO, CNRM A2 at SML, and EH4 B2 at SFO and SML projections are significant above the 95th level, respectively. The duration of extreme events decreases from north-to-south, consistent with the patterns of

variability for extreme occurrences (Figure 8) and extreme events (Figure 9), and with the intensity of the wave climate decreasing from north to south.

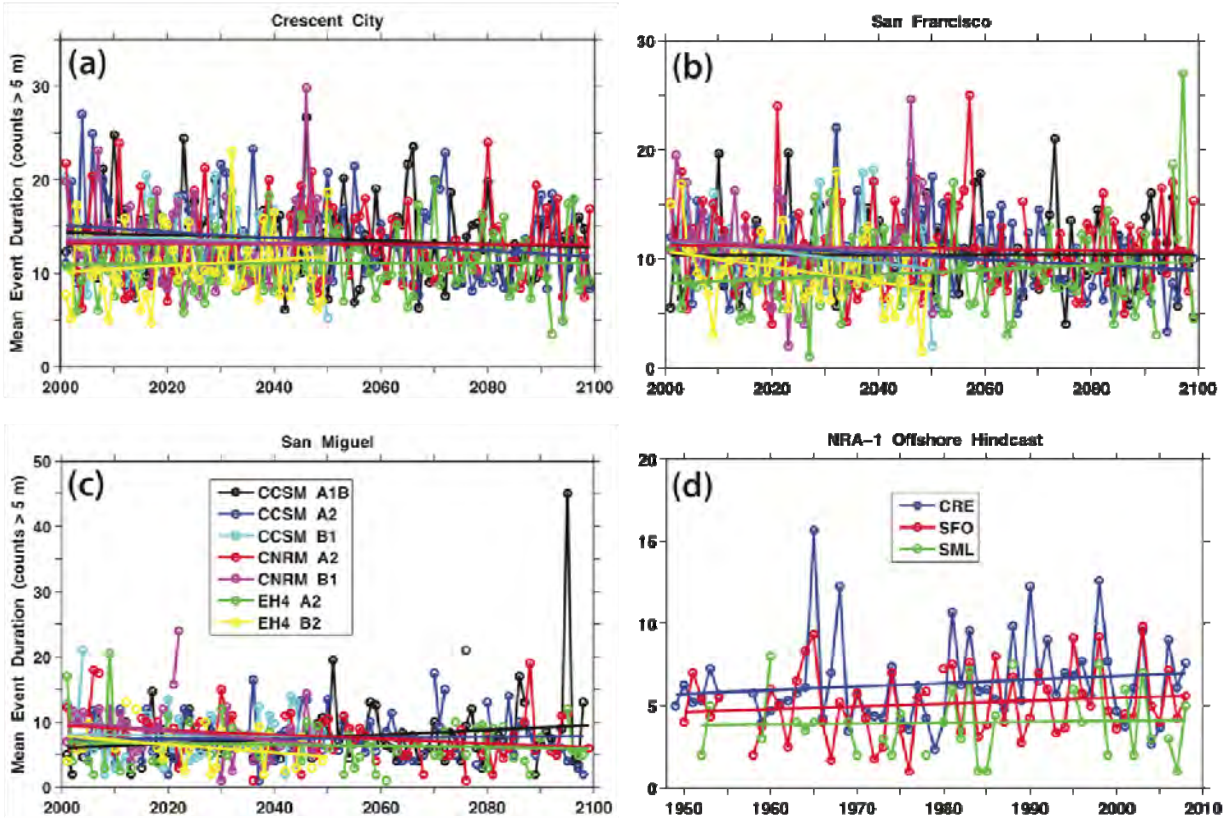


**Figure 10. Mean Duration of Extreme Winter Events. Mean duration that Hs was continuously > than 5 m for at least six hours during Nov.–Mar. winters for projected WW3 model waves forced by GCM winds from the models in Table 1 at offshore locations near (a) Crescent City, (b) San Francisco, (c) San Miguel (see Figure 5 for locations), and (d) hindcast Hs > 5 m at the nearest grid node. Legend in (c) applies to (a) and (b).**

### 2.6.4 Azimuths of Extreme Winter Events

Because the dominant azimuths of extreme wave events are highly variable over particular winters, the median azimuth of all extreme events was chosen to characterize the variability of the most likely extreme wave directions. The projection and hindcast median winter azimuths are progressively more northerly moving from north-to-south along the California coast, consistent with the dominant wave generation region in the eastern North Pacific north of Cape Mendocino. Comparing hindcast estimates with projections, interannual variability over the twenty-first century is expected to be similar to that observed recently.

Of the projections, only the CCSM3 B1 trend at SML is statistically significant, above the 95th percentile level, while none of the hindcast median azimuth trends are, although an upward bias suggests an increasing tendency for more northerly wave azimuths at SML.

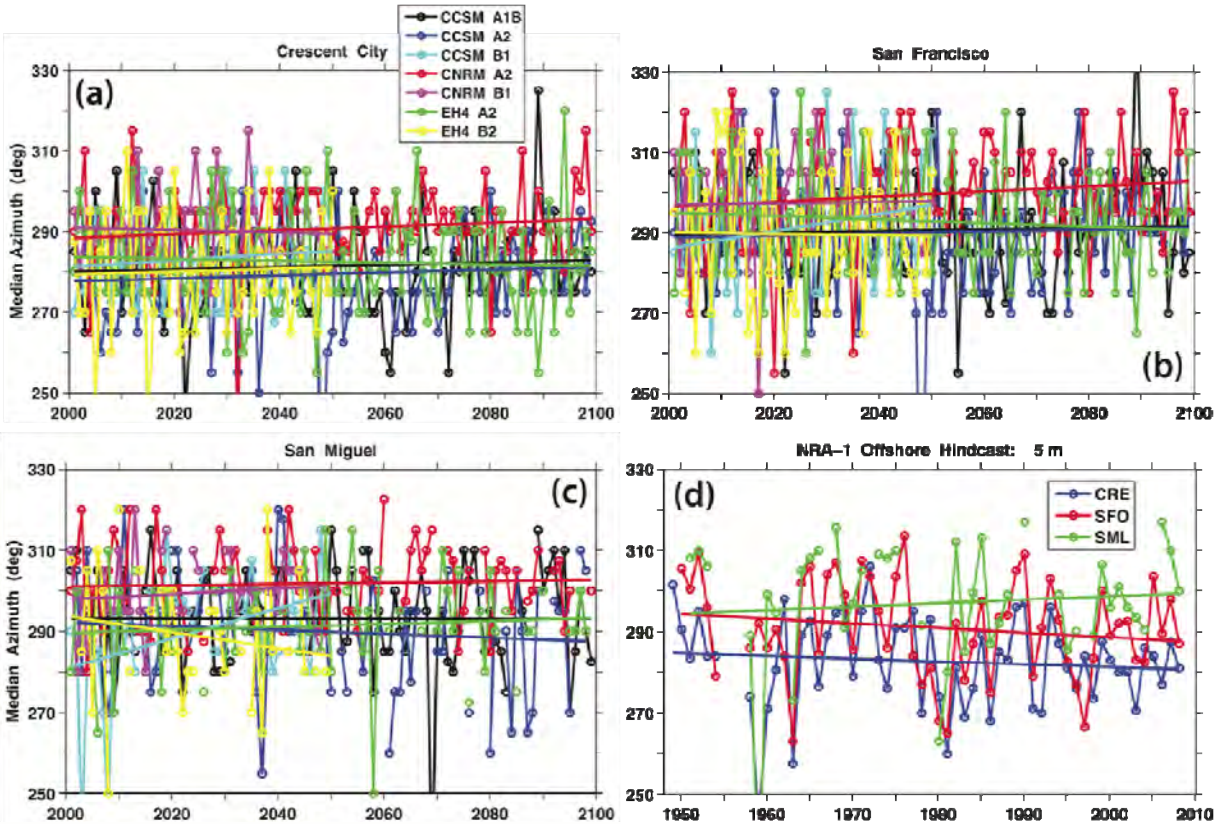


**Figure 11. Winter Medium Azimuth. Median azimuth of all events during Nov.–Mar. winters that Hs was continuously > 5 m for at least 6 hours for projected WW3 model waves forced by GCM winds from the models in Table 1 at offshore locations near (a) Crescent City (CRE), (b) San Francisco (SFO), (c) San Miguel (SML) (see Figure 5 for locations), and (d) hindcast Hs > 5 m. Legend in (a) applies to (b) and (c).**

The coastal impact of particular extreme wave events depends in part on the wave azimuth relative to the norm. Stretches of coastline that are exposed to the typical northerly approaching extreme waves are to some extent "hardened" by being annually impacted by wave events having azimuths greater than 275°. Stretches of coast having a more southerly exposure are to some extent shielded from waves from the north (Graham 2005; Adams et al. 2011). Increased incidence of extreme events with more southerly azimuths could produce a disproportionate impact. Analysis of hindcast extreme Hs events shows that the number of extreme wave events having more southerly azimuths has some relationship with El Niño, as expected (Storlazzi and Griggs 2000; Barnard et al. 2011), particularly noticeable at Crescent City (Figure 12, NRA-1 hindcast), but that tendency is not strong. Evidently, the tendency for greater coastal erosion during strong El Niño southern oscillation (ENSO) episodes (Storlazzi and Griggs 2000) is more dependent on elevated sea levels and high wave energy, as well as their timing with respect to high tide, than wave direction. The dominant wave azimuth in the San Francisco region is typically north of 275°, even during the 1982–1983 and 1997–1998 strong El Niños. The hindcast

extreme Hs events at San Miguel show a dominant northerly azimuth since 1995, consistent with the spatial analysis of the dominant wave generation regions (Figures 3, 4).

Extreme wave event patterns from high-biased (CCSM3) and low-biased (EH4) GCM wind–forced WW3 model Hs simulations for the A2 scenario illustrate the differences between projections, with the CCSM3 projection producing a higher incidence of extreme events than do either the EH4 projection or the NRA-1 hindcast. Comparing statistics of the WW3 projections with the NRA-1 hindcast over the common available data period from 2000–2008 (Table 2) indicates that the CCSM3 means are similar to the hindcast data, but that there is substantially more variability in the GCM wind–forced Hs projection estimates. Interestingly, the hindcast mean is lower than the projections near Crescent City, but higher to the south, indicating more southerly wave generation regions. The changes in Hs mean and standard deviation (std) and mean peak wave period (Tp) are consistent with north-to-south wave propagation being dominant, i.e., the dominant wave azimuth is north of west. This pattern is consistent with the variability along the California coast shown in Figures 3–4 and Figures 6–11.

The incidence and azimuths of extreme Hs events for the EH4 projection more closely resemble the NRA-1 hindcast. However, the CCSM3 and EH4 projections near San Francisco (Figure 12, middle panels) both suggest that the dominant extreme wave azimuth will remain from the north, consistent with Figure 11, and that the incidence of more southerly extreme wave events will not increase over the twenty-first century.

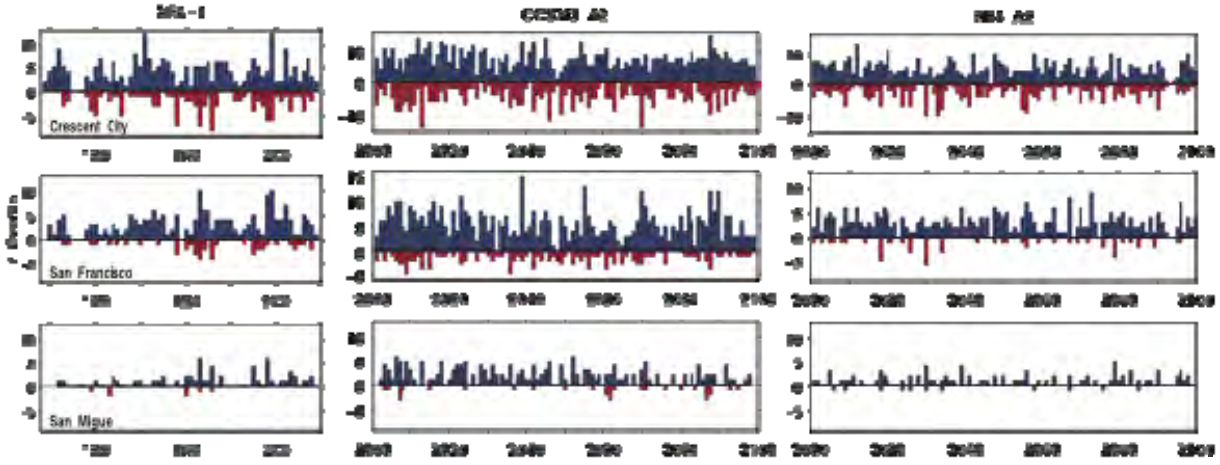


**Figure 12. North vs. South Azimuths of Extreme Events. The number of extreme events with Hs > 5 m having azimuths of respective peak event Hs > 275o (north, blue) or Hs < 275o (west-southwest, red) near Crescent City (top), San Francisco (middle), and San Miguel (near Pt. Arguello, bottom) for WW3 model NRA-1 hindcast (left), CCSM3 A2 (middle), and EH4 A2 (right) GCM-wind WW3 Hs projections.**

**Table 2. Wave Model Hindcast vs. Projections: Offshore Wave Statistics 2000–2008. Wave model (WW3) Hs statistics for hindcast (NRA-1) and GCM wind–forced wave model simulations (with peak wave period (Tp)) for offshore locations near (a) Crescent City, (b) San Francisco, and (c) San Miguel.**

(a)

| Winds | Mean Hs (m) | Hs Std (m) | Mean Tp (s) |
|---|---|---|---|
| NRA-1 | 2.39 | 1.17 | |
| CCSM3 A1B | 2.33 | 1.49 | 10.34 |
| CCSM3 A2 | 2.45 | 1.59 | 10.31 |
| CCSM3 B1 | 2.35 | 1.60 | 10.46 |
| CNRM A2 | 2.11 | 1.48 | 9.80 |
| CNRM B1 | 2.16 | 1.49 | 10.09 |
| EH4 A2 | 1.83 | 1.49 | 8.43 |
| EH4 B2 | 1.84 | 1.49 | 8.18 |

(b)

| Winds | Mean Hs (m) | Hs Std (m) | Mean Tp (s) |
|---|---|---|---|
| NRA-1 | 2.37 | 1.00 | |
| CCSM3 A1B | 2.15 | 1.15 | 10.59 |
| CCSM3 A2 | 2.26 | 1.25 | 10.62 |
| CCSM3 B1 | 2.20 | 1.28 | 10.68 |
| CNRM A2 | 2.01 | 1.20 | 10.04 |
| CNRM B1 | 2.06 | 1.17 | 10.04 |
| EH4 A2 | 1.62 | 1.17 | 9.75 |
| EH4 B2 | 1.61 | 1.20 | 9.60 |

(c)

| Winds | Mean Hs (m) | Std (m) | Mean Tp (s) |
|---|---|---|---|
| NRA-1 | 2.13 | 0.81 | |
| CCSM3 A1B | 1.66 | 0.90 | 10.75 |
| CCSM3 A2 | 1.74 | 0.99 | 10.84 |
| CCSM3 B1 | 1.73 | 1.00 | 10.80 |
| CNRM A2 | 1.68 | 0.91 | 10.07 |
| CNRM B1 | 1.72 | 0.90 | 10.43 |
| EH4 A2 | 1.30 | 0.88 | 10.64 |
| EH4 B2 | 1.30 | 0.92 | 10.71 |

Comparison of CCSM3 A2 and EH4 A2 with the NRA-1 statistics (mean Hs, Table 2) suggests that CCSM3 WW3 projections are closer to historical observations than EH4. However, compared with historic occurrences, the number of extreme events appears to be somewhat overestimated by CCSM3 (Figure 12), suggesting either stronger winds (storms) or closer proximity to the coast. Because calibration of GCM winds and different GCM parameterizations make absolute WW3 model wave characteristics uncertain, their trends have greater weight. Figures 6–12 suggest that wave variability will not change appreciably over the twenty-first century.

## 2.7 Runup

Changes and variability of the coastal flooding potential can be estimated from wave runup, defined as the vertical distance that storm-forced waves travel up a fixed beach slope above SWL. The instantaneous reference SWL is determined from the superposition of RSL, tide, and non-tide water levels. The magnitude of instantaneous storm-forced overtopping runup heights, velocities, and volumes over sea walls, roads, parking lots, and other coastal structures near the ocean's edge (flooding) are dependent on wave characteristics, as well as the instantaneous sea level elevation. Runup depends on nearshore wave height, wave period, and beach slope (eqn. (19), Stockdon et al. (2006)), used to compute runup values herein. A fixed 2 percent beach slope at all locations was chosen so that runup comparisons could be made between locations based on wave and sea level states, recognizing that beach slopes can vary considerably along the California coast. Because short-term fluctuations in coastal California water levels associated with storm events are dominated by diurnal and semi-diurnal tides, coastal flooding generally occurs near high tide under extreme wave conditions.

In a "no sea level rise" scenario (Figure 13), extreme runup variability follows the general trends in extreme wave variability for the wave scenarios shown in Figures 6 and 7. In the SC region, the low-energy wave climate results in a regime where tides are relatively more important. Only the CNRM A2 trend at La Jolla is significantly different from zero above the 90th percentile level. The mean of the extreme winter runup from Ocean Beach north is similar for all models. Notable differences between extreme winter runup estimates near San Francisco and near Crescent City during common winters can be attributed to differences in wave amplitude, period, and azimuth. Similar differences are reflected in offshore and nearshore wave variability (Figures 6 and 7). Lower mean-extremes at Santa Cruz and La Jolla relative to Ocean Beach and South San Diego emphasize the importance of near-coastal bathymetry and wave direction, as well as shielding by coastline geometry relative to the dominant wave direction, on runup and associated flooding potential at particular locations. However, the lack of significant trends in extreme runup projections is consistent with little change in flooding potential along the California coast if RSL remains relatively stationary.

The superposition of tide and non-tide fluctuations on associated Vermeer-Rahmstorf (2009) MSL rise projections (Figure 14), giving the combined SWL, increases runup heights towards the end of the twenty-first century by about the projected Vermeer-Rahmstorf MSL rise projections (Figure 1). The MSL rise factor about doubles runup levels at 2100 compared with current RSL, substantially increasing flooding potential. Note the relative difference in extreme means, represented by the trends, between Ocean Beach and Crescent City for the low GHG scenarios likely results from spatial variability within and between the GCM model outputs. Runup extreme curves with lower variance, i.e., at Santa Cruz and La Jolla, are indicative of low wave energy regimes and that extreme runup at these locations has a stronger tidal dependency.

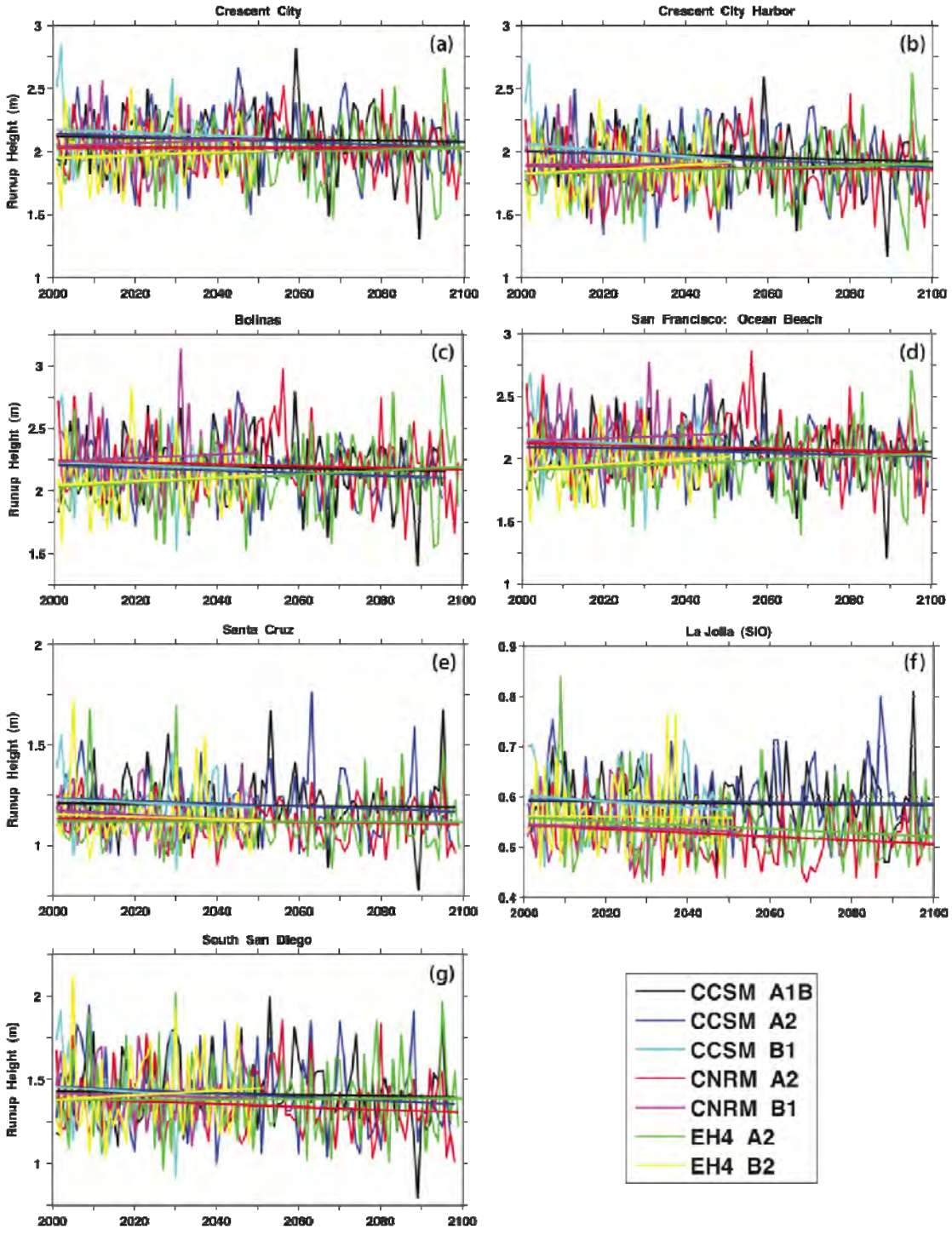


**Figure 13. Extreme Runup Projections – Constant Sea Level. Extreme winter (Nov.–Mar.) 99th quantile runup projection levels using the empirical Stockdon (2006) runup relation for a fixed 2% beach slope. These projections do not include sea level rise, tide, or non-tide projections.**

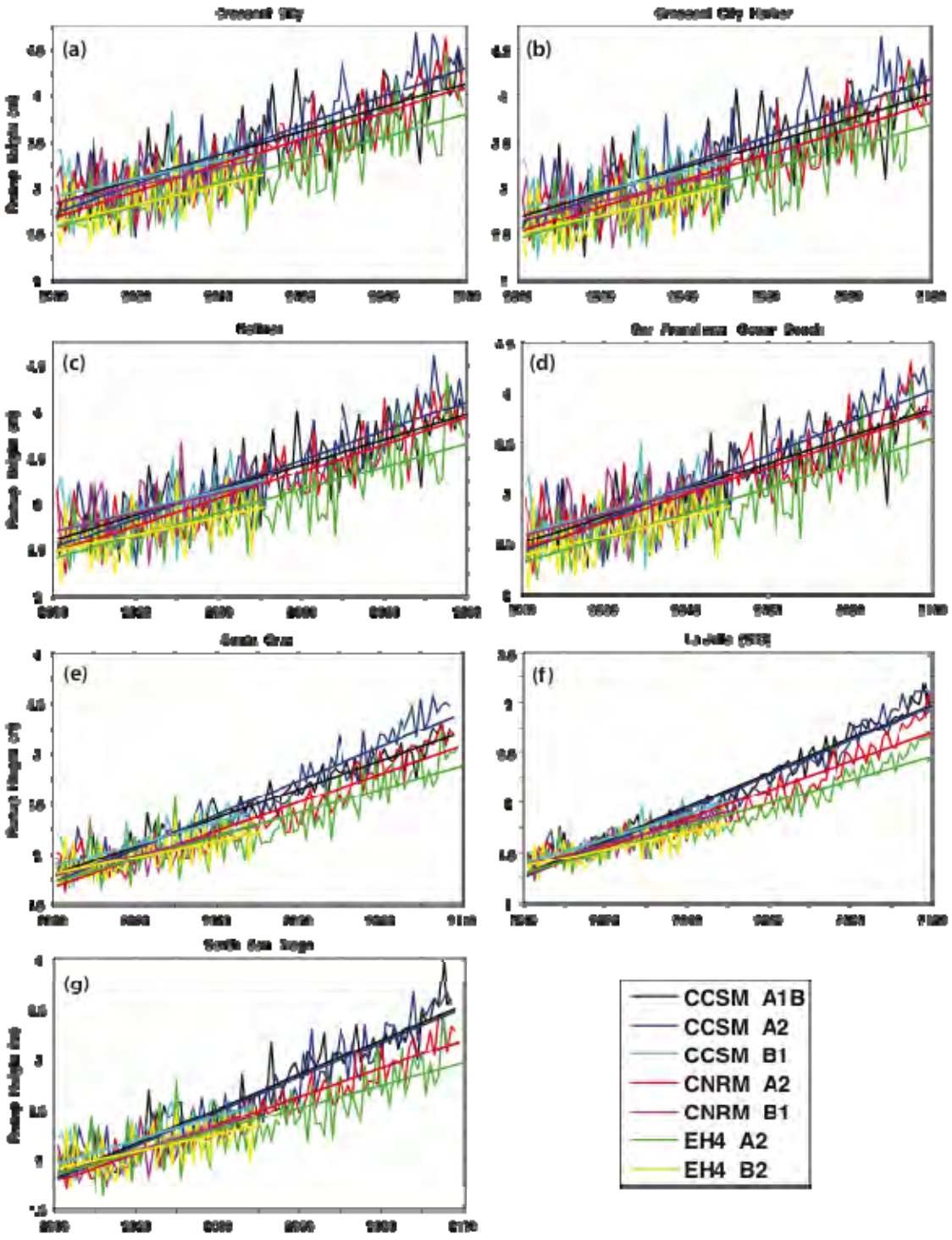


**Figure 14. Extreme Runup Superimposed on Vermeer-Rahmstorf Sea Level Projections. Extreme winter (Nov.–Mar.) 99th quantile runup projection levels using the empirical Stockdon (2006) runup relation for a fixed 2% beach slope. These curves include Vermeer-Rahmstorf (2009) MSL rise, tide, and non-tide projections.**

### 2.7.1 Winter Extreme Occurrences

The frequency and temporal variability of extreme runup events characterizes changes in flooding potential. Runup levels include storm surge and tide variability, as well as wave variability. Additionally, the application of wave transformation matrices necessarily causes runup levels to also include the wave direction factor. Thus, because extreme runup levels are location specific, extreme runup thresholds that signify changes in flooding potential must be determined on a site-specific basis. Nonetheless, runup projections at representative high and low wave energy locations in the northern, central, and southern California regions can be used to describe general tendencies of changes in flooding potential along the California coast.

Substantial variability of extreme runup levels between locations is observed, as indicated by the range of mean 99th quantile extreme threshold levels for all seven GCMs (annotated in Figures 15a–g.) The 99th quantile estimates for all GCMs are within about 10 percent of these mean values at each location, showing consistency between the GCMs. These location-specific mean extreme levels have similar values at San Francisco Ocean Beach and northward. However, the much lower value at Santa Cruz underscores the importance of wave transformation resulting from local bathymetry and sheltering from local coastal geometry. The importance of these factors is underscored by the difference between extreme runup levels at La Jolla and South San Diego near the U.S.-Mexican border, where wave heights are significantly higher (see Figure 7) even though the dominant wave direction is from the north (Figures 11c,d; Figure 12). At the two southernmost locations near San Diego and at the Santa Cruz Boardwalk, a few winters having many occurrences above the mean winter activity, characterized by the trend line, raises mean winter extreme occurrence levels close to the higher wave energy locations near San Francisco and Crescent City.

In general, the last 2–3 decades of the twenty-first century show a decrease in the occurrence of extreme runup levels at all locations, suggesting decreasing flooding potential if coastal sea levels remain stationary. Most trends are not significant, with the exception of the CNRM A2 and CCSM3 A2 trends at La Jolla and San Francisco, Ocean Beach, respectively, above the 95th percentile level.

Inclusion of Vermeer-Rahmstorf MSL rise projections significantly increases the incidence of winter runup extremes relative to the stationary sea level runup 99th quantile by a factor of 5 or more at the end of the twenty-first century, substantially increasing the flooding potential risk (Figure 16). The differences between the ECHAM4-OPYC (EH4) model and the CCSM3 and CNRM models becomes apparent under rising RSL, with the EH4 models about 30 percent lower and exhibiting substantially higher variance. Linear trend lines give a rough estimate of mean occurrence levels for comparisons between models. Rising RSL has the greatest impact at the three lowest wave-energy locations at Santa Cruz, La Jolla, and South San Diego that are more tide-dominated, increasing the tide range and thus causing a greater increase in the number of extreme runup occurrences than at high wave energy locations where higher tide levels contribute a relatively smaller percentage to the total runup estimates.

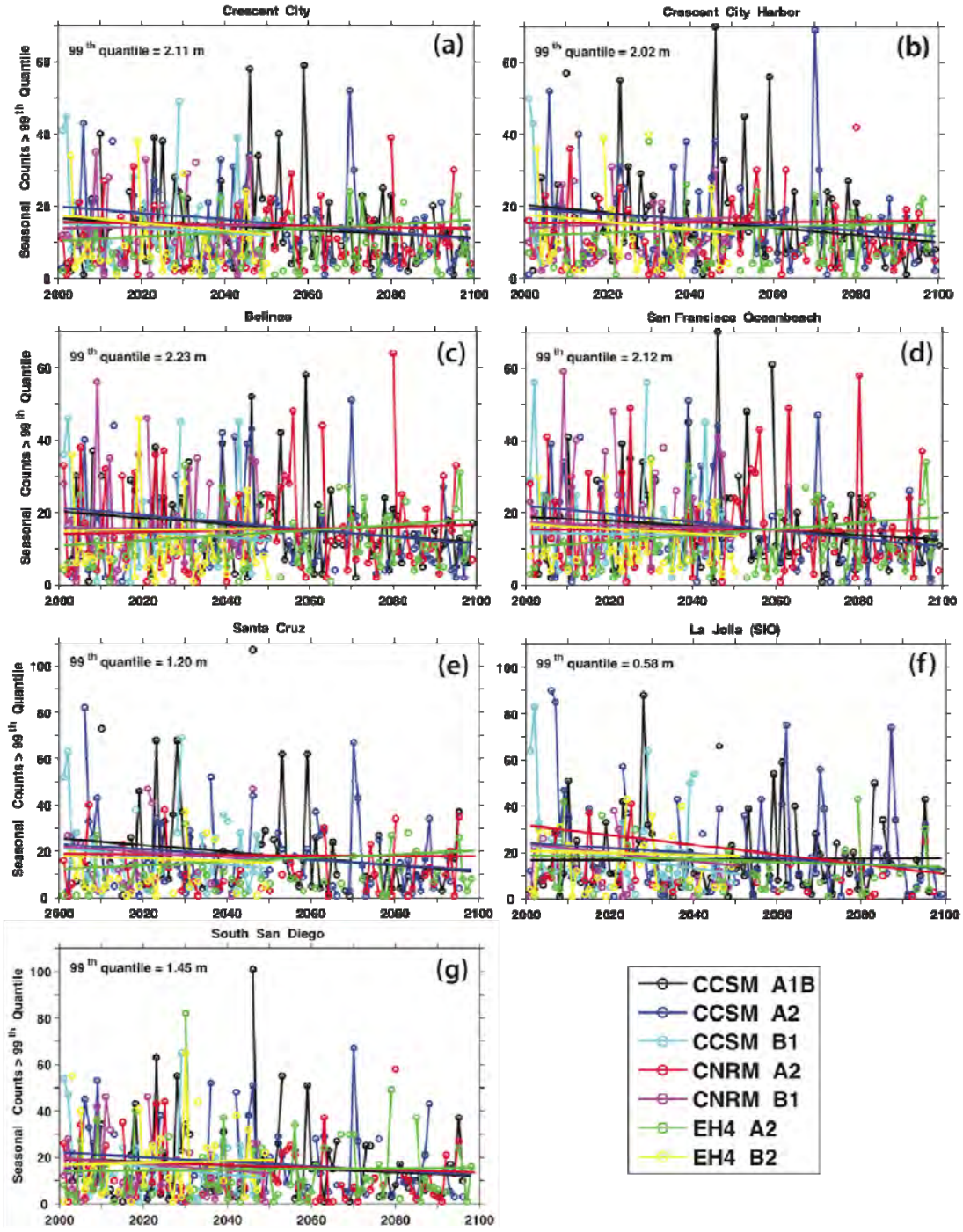


**Figure 15. Projected Winter Extreme Runup Occurrence. Number of extreme winter (Nov.–Mar.) runup realizations that exceed the 99th quantile runup projection level over the twenty-first century for a fixed 2% beach slope, not including sea level rise. The mean of the 99th quantile level for all seven models at respective locations is annotated. The legend applies to all panels. Note that vertical scales in (a)–(d) differ from (e)–(g).**

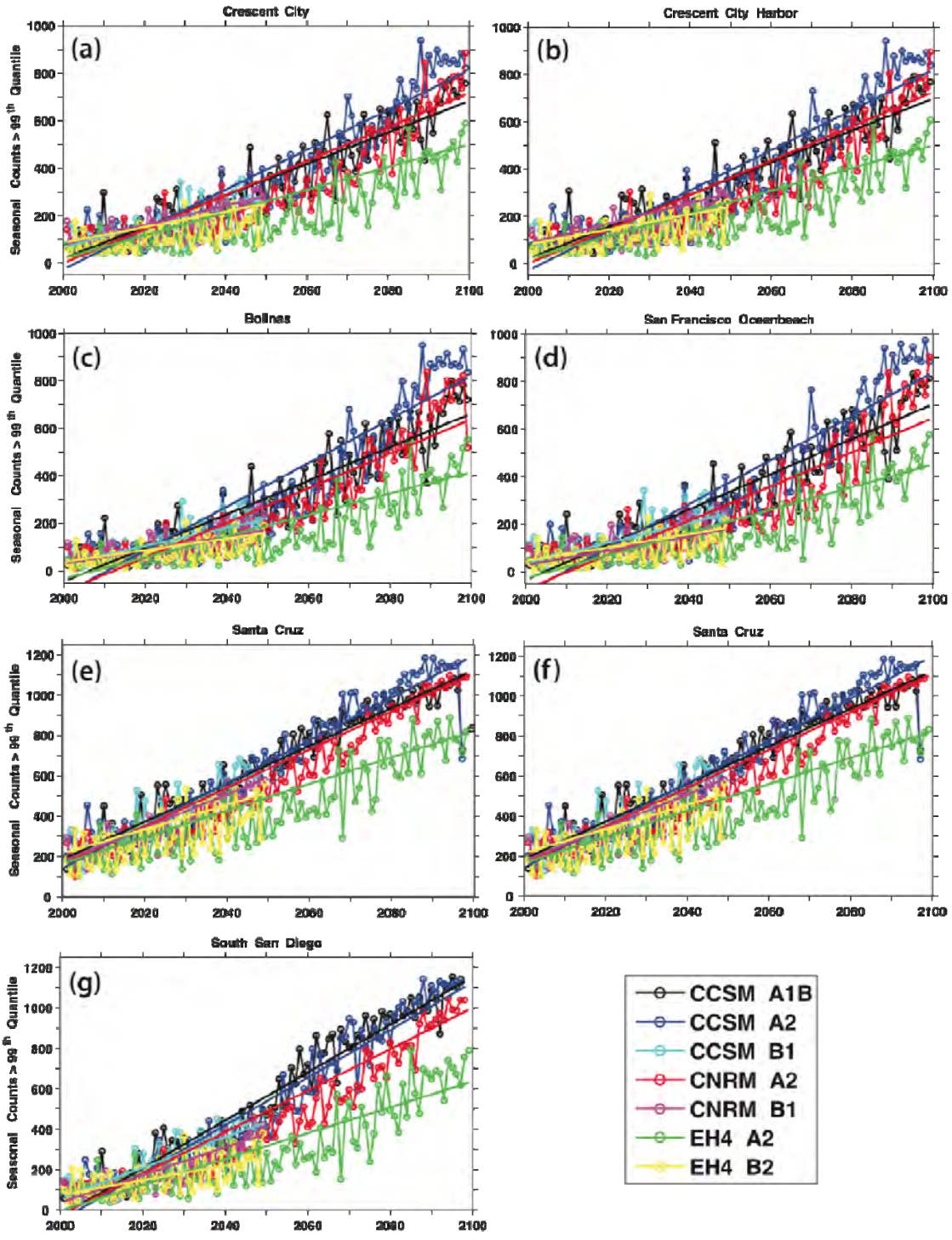


**Figure 16. Projected Winter Extreme Runup Occurrence: Including VR SLR Projections. Number of extreme winter (Nov.–Mar.) runup realizations over the 21st century that exceed the no-sea level rise 99th quantile runup projection levels for a fixed 2% beach slope; these estimates include Vermeer-Rahmstorf MSL rise projections. The legend applies to all panels. Note that vertical scales in (a)–(d) differ from (e)–(g).**

## 2.8 Return Periods from Joint Probability

The changes in flooding potential associated with different sea level rise projections can be estimated by their effect on return periods of runup heights determined from the joint probability of runup and sea level height. The greatest potential for coastal flooding occurs when extreme wave conditions occur near high tide. Because extremes in non-tide fluctuations increase with latitude (Bromirski and Flick 2003), their importance rises northward along the California coast. Changes in the return period of particular runup levels give an indication of changes in flooding potential. To assess the impact of RSL rise on flooding potential, return period curves were determined from the joint probability of the combination of tide plus non-tide water levels with and without RSL rise included, with the global VR MSL rise projections used for RSL.

The joint probability of wave-driven runup and sea level was estimated using the methodology of Pugh and Vassie (1980). In this method, the probability density functions (PDFs) for the runup and sea level parameters are first determined. The instantaneous water level (SWL) and its components (tide, non-tide, and RSL) are determined independent of runup. The joint PDF is obtained from the convolution of respective sea level PDF components. Non-tide and/or tide height can be superimposed sea level rise estimates to obtain the effective instantaneous SWL PDF of their combination for convolution with either nearshore wave-height or runup. The resulting joint PDFs were filtered to account for irregularities in the tide gauge, GCM, and wave model data. The joint PDFs give the probability of occurrence of all possible combinations of runup with the respective sea level components used to obtain the joint PDF; i.e., all possible combinations of runup above the effective SWL.

The cumulative probability density function (CPDF) of the joint PDF is then used to obtain the associated return periods of occurrence of total runup heights (flooding potential, which includes SWL) at a specified water-level sampling density (bin width); here 1 cm bin widths were used. Return period curves obtained from the joint CPDFs give the return period for each of the combined water levels with runup (Figure 17). Considering the uncertainties in the GCM outputs used to generate both waves and non-tide fluctuations, more sophisticated methods for estimating return periods of the joint occurrence of associated extremes (e.g., Mendez et al. 2007) are generally unwarranted.

As demonstrated above, non-tide water levels are not expected to increase significantly above twentieth-century levels. Consequently, any changes in flooding potential, i.e., increases in the occurrence and magnitude of coastal flooding events, will be primarily dependent on RSL rise. To assess the impact of RSL rise on flooding potential, return period curves were determined for the following:

- No RSL rise, the mean state since about 1980 (Bromirski et al. 2011)
- The global altimetry MSL rise rate since 1992 of 3 mm/yr
- Representative high (CCSM3-A2) and low (EH4-A2) Vermeer-Rahmstorf global MSL rise projections

Comparison of return period curves (Figure 17) of the no sea level rise (SLR) and altimetry SLR scenarios with those that include Vermeer-Rahmstorf (VR) SLR projections indicate that, for example, current 100-year return period events will potentially occur at least annually along the entire California coast near the end of the twenty-first century, even for the lowest of the A2 scenario projections. Changes in return periods are most pronounced at La Jolla in SC region (Figure 17e), exemplified by the greater difference in runup return periods that include the VR projections (thick) and those that do not (thin and dashed curves), compared with other locations. About a 125 cm difference in annual runup levels between the high- and low-wave energy locations (Figure 17a–c and Figure 17d–e, respectively) is observed. The 1982–83 El Niño possibly produced the greatest coastal impacts during the twentieth century; i.e., a 100-year return period winter that could be represented by the no RSL rise curves (thin solid lines, Figure 17). Comparison of the no RSL rise curves with those for both CCSM3 and EH4 VR MSL projections indicates that, at the end of the twenty-first century, such events are projected to occur annually.

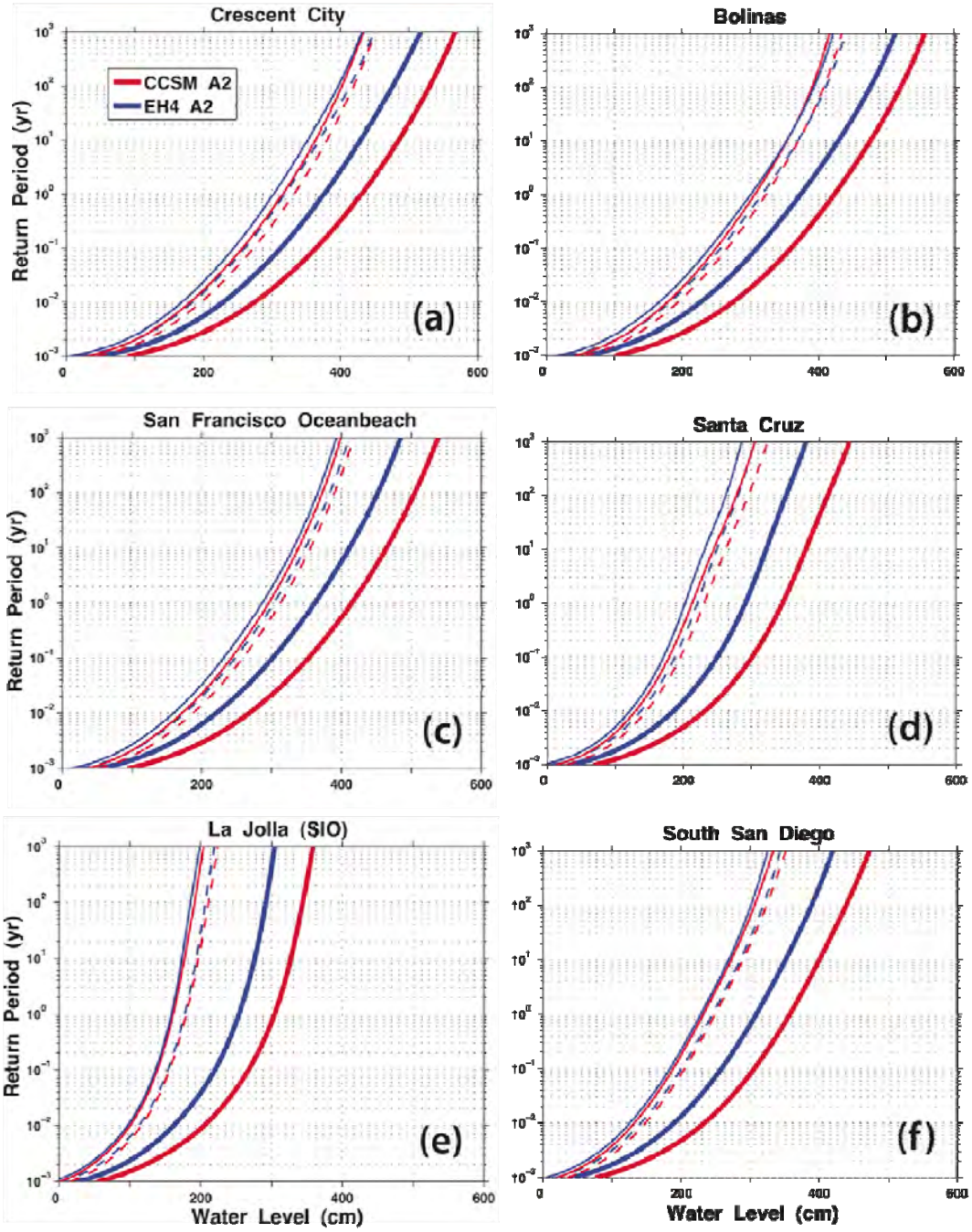


**Figure 17. Sea Level Rise Effect on Runup Return Period. Return period curves for the joint probability of runup with tide and non-tide components for no RSL rise (thin solid), the altimetry rise rate of 3 mm/yr (thin dashed), and Vermeer-Rahmstorf (VR) global MSL rise (thick curves). The runup at each location was determined using a 2% beach slope and transformed nearshore wave conditions. Return periods were determined from the joint probability of runup for respective sea level rise projections for the CCSM3 and EH4 A2 GCM realizations, spanning the general range of the A2 GHG scenarios.**

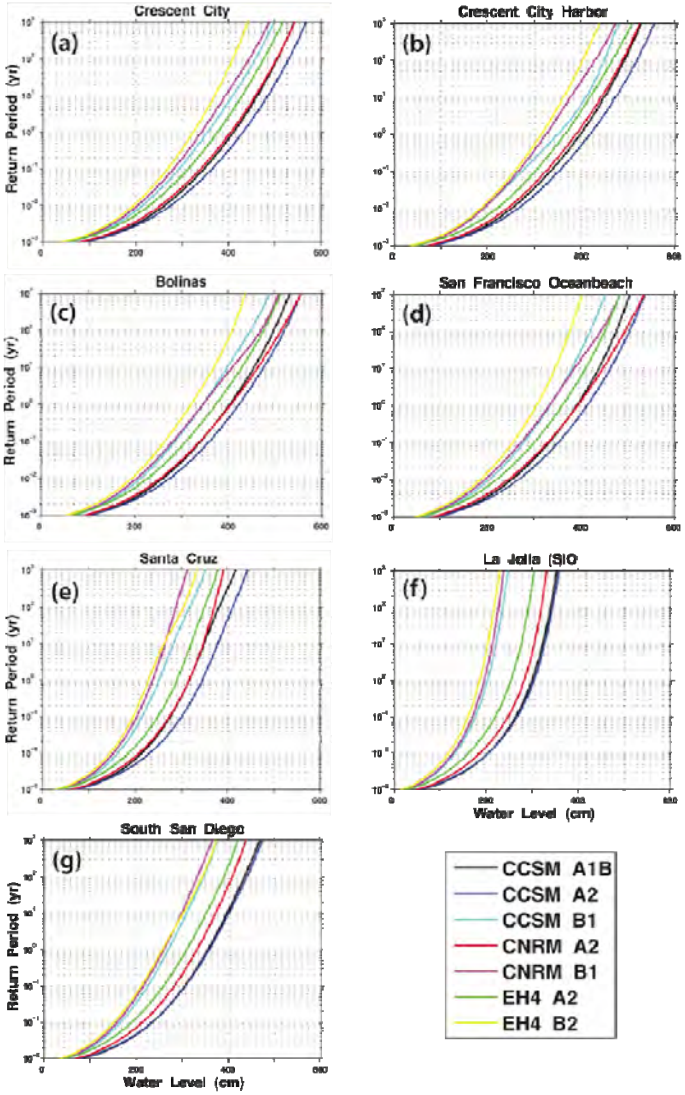


**Figure 18. Return Period Curves. Return period curves for the joint probability of runup and the total instantaneous SWL. The runup at each location was determined using a 2% beach slope. Runup was computed for nearshore wave and sea level conditions forced by waves superimposed on SWL, incorporating tide+non-tide+Vermeer-Rahmstorf global MSL rise components for the seven GCM realizations (legend; Table 1). These return period panels include the SWL curves in Figure 14.**

Return period curves derived from the joint probability of SWL and runup for the seven GCM simulations at the seven coastal locations (Figure 18) emphasize the importance of both nearshore wave height and SWL on runup levels. Higher runup generally indicates a higher flooding potential. Similar to that shown in Figure 17, runup levels at the one-year return period for the seven models span about 125 cm, showing significant variability between the models at each location that is largely controlled by differences in their respective Vermeer-Rahmstorf MSL projections, which is included in SWL. Differences between relatively nearby

locations also emphasize the importance of nearshore wave conditions, determined by the deep-water offshore-to-nearshore MOP wave transformation matrices.

### 2.8.1 Effect of Beach Slope on Flooding Potential Projections

In addition to the impact of antecedent storm activity during each winter, beach slope varies on both interannual and longer time scales, controlled in part by long-term changes in wave climate, longshore currents, and summer wave characteristics as well as RSL. Beach slope also depends in part on local and nearby geology, which determines beach composition (grain size, which affects the response to wave activity) and depth above the substrate. Beach slope is generally proportional to grain size, with steeper slopes associated with larger grain size (Shepard 1963). Steeper beach slopes give higher runup levels, typically dissipating the wave energy over a shorter horizontal distance. Because future beach slopes used for flooding potential projections are indeterminant for particular events, the sensitivity of flooding potential to beach slope needs to be considered.

The slope factor was investigated by computing return period curves for a suite of foreshore beach slopes (Figure 19) for a zero RSL rise trend, analogous to recent observations (Figure 20). The shapes of the joint CPDF curves are strongly affected by the inclusion of increasing RSL (not shown), resulting in significant differences in respective return period curves (Figure 17). Beach slope can vary considerably along the California coast depending on local geomorphology and season, e.g. winter beach slopes can be considerably steeper than during summer at the same location after finer grained sands are removed by winter wave activity. Return period curves for the other GCM scenarios and locations shown in Figure 18 display similar variability with beach slope, with the La Jolla (SIO) curves much steeper with a narrower range (especially between the 75th and 99th percentiles), reflecting conditions in the SC region where wave energy is lower and the tide is relatively more important.

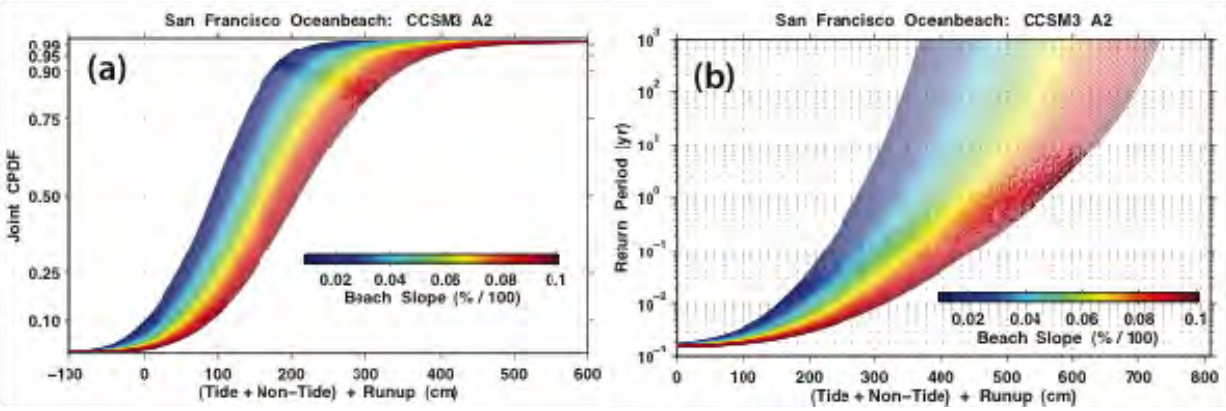


**Figure 19. Sensitivity of Return Period to Beach Slope. (a) Joint cumulative probability density functions (CPDF) over 2000–2099 for no sea level rise determined for a spectrum of foreshore beach slopes. All curves were computed for the same nearshore wave, tide, and non-tide sea level conditions forced by CCSM3 A2 GCM wind fields. (b) Return period curves for the CPDFs in (a).**

# Section 3: Summary and Conclusions

Identification of changes in coastal flooding incidence depends in part on recognition of the past history at particular locations. Low-lying coastal locations that are prone to flooding (and those in jeopardy) will be more affected as sea level rises. Because storm activity is not projected to intensify or appreciably change the characteristics of winter nearshore wave activity over the twenty-first century, the dominant factor controlling any increased flooding potential and associated coastal erosion will be rising RSL, which affects high-tide levels. Rising RSL allows more wave energy to reach farther shoreward, exacerbating coastal erosion and increasing flooding potential.

This paper focuses on oceanographic factors, primarily changes in RSL and waves, that affect flooding potential along the California coast. However, factors associated with tectonic processes (earthquakes, differential uplift) could produce co-seismic vertical land displacements that affect RSL. Subsidence of artificial fills and mud around bays and estuaries can result in effective RSL rise at particular locations, an important consideration in the San Francisco Bay/Delta region (Burgmann et al. 2006). Also, while the chance of flooding from tsunamis is low, mega-earthquakes at the Alaska and Cascadia subduction zones (Atwater et al. 1995) could generate tsunamis that result in catastrophic coastal flooding events. Other factors, such as sediment supply to buffering beaches and longshore sediment transport and deposition, can also affect flooding potential. Although beyond the scope of this paper, these considerations should not be overlooked.

If the general wave climate remains approximately the same, as wave model projections suggest, or decreases because of a northward shift in storm track, then increases in the frequency and degree of inundation are primarily dependent on RSL. Because extreme event occurrence and duration (Figures 9 and 10) are not expected to change significantly, the timing of extreme wave events with high tide should also not change. The uncertainty in all parameters (except astronomical tide variability) affects estimates of changes in flooding potential (runup). Wave projections incorporate statistical GCM-derived wind-field calibration adjustments that affect wave model Hs, and wave directional spectra from WW3 have uncertainties resulting from GCM winds and WW3 grid spacing. MOP wave transformation matrices depend in part on the reliability of near-coastal bathymetry, which is assumed to be stationary and sufficiently well described. Although storm surge (non-tide water level) is a relatively small component of total instantaneous water levels, that contribution can be critical for flooding if extreme storm waves arrive near high tide. Surge projections are also derived from GCM outputs, and have associated uncertainties. Together, these uncertainties make estimates of absolute values of GCM-projected runup (flooding potential) somewhat less significant than their trends and changes in their variability over the twenty-first century. However, these have been demonstrated to not vary substantially from historic patterns.

RSL along the West Coast provides the base level upon which other shorter-term fluctuations are superimposed. However, ENSO-related extremes, e.g., during the strong El Niños of 1940–1941, 1958–1959, 1982–1983, and 1997–1998, produce the highest amplitude interannual fluctuations at San Francisco (Figure 20b) with magnitudes comparable to the total change in

RSL along the West Coast over the twentieth century. These fluctuations are associated with poleward-propagating, coastally-trapped, Kelvin-type waves and warm tropical water, as well as with teleconnections that affect storm patterns and intensity across the basin. Thus, because trends in ocean wave extremes and storm-forced non-tide fluctuations are not expected to change significantly over the twenty-first century, upward trends in RSL will be the dominant factor affecting any increase in the frequency or magnitude of coastal flooding along the California Coast.

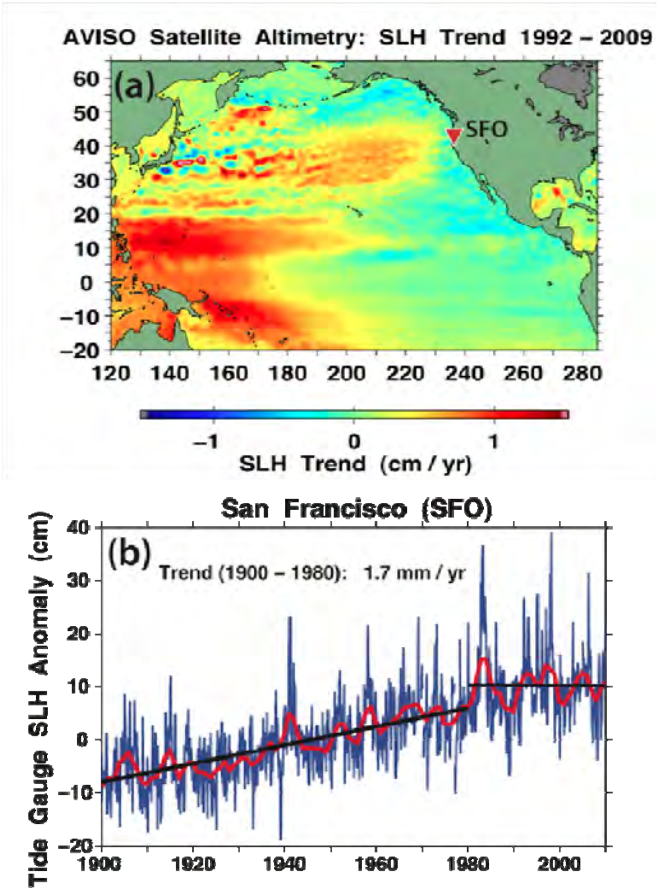


**Figure 20. Observed Trends. (a) Least squares trends in satellite altimetry sea level height (SLH) across the North Pacific basin over the 1992–2009 time period (after Bromirski et al. 2011). (b) Observed tide-gauge sea level monthly anomalies, with 3-yr running means (red lines) at SFO. Note the near-zero trend along the U.S. West coast in (a) that is reflected in the SFO tide gauge record since about 1980.**

## 3.1 RSL Response to Broad-scale Ocean Circulation Changes

Satellite altimetry suggests that global MSL rise rate has increased about 50 percent since the early 1990s to about 3 mm/yr (Cazenave and Nerem 2004), with the rate of MSL rise varying significantly across the Pacific basin (Figure 20a) (Bromirski et al. 2011; Merrifield 2011). Tide

gauge estimates of RSL trends (Figure 20b), confirmed by satellite altimetry since 1992, indicate no statistical increase in sea levels along the California coast since about 1980. In contrast, prior to the mid-1970s regime shift (Miller et al. 1994), San Francisco tide gauge measurements indicate that California coastal sea levels rose near the global rate of about 2 mm/yr over the 1930–1975 epoch (Figure 20b).

Sea level trends observed along the California coast can be significantly different than the rate of MSL rise. Local RSL is the base level on which shorter duration fluctuations (such as El Niño–related increases, tides, storm surge, and waves) are superimposed. RSL along the California coast depends on influences of the Pacific decadal oscillation (Mantua et al. 1997) on associated basin-scale ocean circulation affecting North Pacific sea levels, as well as on MSL rise. The canonical PDO warm- and cold-phase sea level patterns have associated wind patterns (Mantua 2011).

Sea levels along the California coast depend in part on the dynamical response of the ocean to regional winds over the eastern boundary of the North Pacific. The expected PDO-related sea level response along the California coast can be modulated by regional wind stress patterns. In general, the warm phase of the PDO is associated with elevated coastal sea surface temperature (SST) and regional winds that favor rising coastal sea levels (Mantua et al. 1997). However, since about 1980, the eastern boundary regional wind stress patterns have been opposite to that expected for the warm phase of the PDO, resulting in upwelling instead of downwelling conditions prevailing along the eastern boundary (Bromirski et al. 2011). This has suppressed the eastern boundary RSL rise expected during the PDO warm phase (i.e., relatively warm coastal waters with an associated steric response that would raise RSL).

Mean wind stress over the entire North Pacific basin recently reached levels not observed since before the mid-1970s regime shift (Bromirski et al. 2011). This change in broad-scale wind stress patterns is associated with an apparent shift of the PDO to its cold phase, having associated colder eastern boundary SST (relatively colder, denser water), which should continue to suppress California coastal RSL. Again, regional wind stress patterns can modulate the expected RSL response in either direction. But the net effect will likely be that RSL rise will, for now at least, continue to be significantly less than global MSL rise. However, as global MSL rises, there eventually must be a sea level height adjustment that results in an increase in RSL along the California coast. The relationship of California coastal RSL to MSL will become increasingly important if MSL rise accelerates in association with projected increases in surface air temperature towards the end of the twenty-first century (Bindoff and coauthors 2007).

The importance of persistent regional wind patterns has also been demonstrated to contribute significantly to RSL rise-rates in the western tropical Pacific (Figure 20a) that greatly exceed the global altimetry MSL trend (Merrifield 2011; Bromirski et al. 2011), attributed by Merrifield (2011) to a steady increase in the trade winds since the early 1990s. Merrifield speculates that the trade wind spin-up is associated with an intensification of north-south Hadley cell atmospheric circulation, which is linked to an associated increase in mid-latitude westerlies and equatorward winds along the Pacific coast of North America, consistent with the eastern boundary wind regime identified by Bromirski et al. (2011). However, weakening and poleward

expansion of Hadley circulation are anticipated under global warming (Lu et al. 2007). This could reduce trade wind strength and cause broad-scale ocean circulation changes that result in a redistribution of western North Pacific ocean waters across the basin and raise sea levels along the West Coast. Although Merrifield (2011) found no association of the elevated western Pacific sea levels with the PDO, the recent changes in wind patterns over the North Pacific may affect Hadley cell circulation and RSL trends across the basin.

Future RSL changes will depend on the magnitude of changes in the PDO, the trade wind mode identified by Merrifield (2011), as well as other regional anomalies in wind forcing noted by Bromirski et al. (2011). While regional wind forcing is difficult to forecast on climate time scales, the recent apparent shift of the PDO index from a positive to a negative phase will likely cause substantial changes in North Pacific winds, which will likely affect regional sea level trend patterns. The dynamics of the forcings that control Hadley cell intensity (and expansion and contraction) may be related to North Pacific decadal variability and to decadal oscillations of the tropical Pacific. Because increased flooding potential along the California coast is expected to be largely be determined by increases in RSL, understanding both regional and gyre-scale responses of the North Pacific ocean-circulation to changes in Hadley circulation are crucial factors to anticipate the magnitude and timing of potential increases in RSL along the California coast.

It is important for coastal managers to avoid being lulled by the relatively stationary mean state of RSL along the California coast since about 1980, which has produced largely manageable impacts from storm events. Although prevailing conditions associated with the apparent shift of the PDO to its cold phase should continue to suppress RSL rise, this cannot continue indefinitely. Eventually, effective RSL rise will likely reach the global MSL rise rate or higher. If the Vermeer-Rahmstorf global MSL rise projections are realized, at the end of the twenty-first century coastal managers can anticipate that coastal flooding events of much greater magnitude than those during the 1982–83 El Niño will occur annually.

# References


Adams, P. N., D. L. Inman, and N. E. Graham. 2007. "Southern California deep-water wave climate: Characterization and application to coastal processes." *J. Coastal Res.* **24**(4): 1022-35.

Adams, P. N., D. L. Inman, and J. L. Lovering. 2011. "Effects of climate change and wave direction on longshore sediment transport patterns in Southern California." *Climatic Change* (in press), doi:10.1007/s10584-011-0317-0.

Atwater, B. F., A. R. Nelson, J. J. Clague, G. A. Carver, D. K. Yamaguchi, P. T. Bobrowsky, J. Bourgeois, M. E. Darienzo, W. C. Grant, E. Hemphill-Haley, H. M. Kelsey, G. C. Jacoby, S. P. Nishenko, S. P. Palmer, C. D. Peterson, and M. A. Reinhart. 1995. "Summary of coastal geologic evidence for past great earthquakes at the Cascadia subduction zone." *Earthquake Spectra*, **11**(1), 1-18.

Aviso. 2010. Ssalto/Duacs multimission altimeter products. http://www.aviso.oceanobs.com/en/data/product-information/duacs/.

Barnard, P. L., J. Allan, J. E. Hansen, G. M. Kaminsky, P. Ruggiero, and A. Doria. 2011. "The impact of the 2009-2010 El Nino Modoki on U.S. West Coast beaches." *Geophys. Res. Lett*., **38**, L13604, doi:10.1029/2011GL047707.

Bindoff, N. L., and coauthors. 2007. *Observations: Oceanic climate change and sea level, Climate Change 2007: The Physical Science Basis,* S. Solomon et al., Eds., Cambridge University Press, 385–432.

Bromirski, P. D. and R. E. Flick. 2003. "Variability of storm-forced extreme sea levels along the U.S. West Coast." *Proc. OCEANS 2003 MTS/IEEE Conf*., San Diego, **2**, 974-978, doi: 10.1109/OCEANS.2003.1283336.

Bromirski, P. D., and R. E. Flick. 2008. "Storm surge in the San Francisco Bay/Delta and nearby coastal locations." *Shore & Beach*. **76**(3): 29–37.

Bromirski, P. D., R. E. Flick, and D. R. Cayan. 2003. "Storminess variability along the California coast: 1858–2000." *J. Clim.*, **16**(6): 982–993.

Bromirski, P. D, D. R. Cayan., and R. E. Flick. 2005. "Wave spectral energy variability in the northeast Pacific." *J. Geophys. Res*., **110**, C03005, doi:10.1029/2004JC002398.

Bromirski, P. D., R. E. Flick, and N. Graham. 1999. "Ocean wave height determined from inland seismometer data: Implications for investigating wave climate changes in the NE Pacific." *J. Geophys. Res - Oceans.*, **104**(C20), 20,753–20,766.

Bromirski, P. D., A. J. Miller, R. E. Flick, and G. Auad. 2011. "Dynamical suppression of sea level rise along the Pacific coast of North America: Indications for imminent acceleration." *J. Geophys. Res. – Oceans*,**116**, C07005, doi:10.1029/2010JC006759.

Burgmann, R., G. Hilley, A. Ferretti, F. Novali. 2006. "Resolving bertical tectonis in the San

Francisco Bay area from permanent scatterer InSAR and GPS analysis." *Geology*, **34**(3), 221-224.

Caires, S., A. Sterl, J. R. Bidlot, N. Graham, and V. Swail. 2004. "Intercomparison of different wind-wave reanalyses." *J. Climate*, **17**, 1893–1913.

Cayan, D. R., P. D. Bromirski, K. Hayhoe, M. Tyree, M. Dettinger, and R. E. Flick. 2008. "Climate change projections of sea level extremes along the California coast." *Climatic Change* doi: 10.1007/s10584-007-9376-7.

Cayan, D. R., M. Tyree, D. Pierce, and T. Das, (2012): Climate and Sea Level Change Scenarios for California Vulnerability and Adaptation. Paper for the California Vulnerability and Adaptation Study. Public Interest Energy Research Program California Energy Commission.

Cazenave, A., and R. S. Nerem. 2004. "Present-day sea level change: Observations and causes." *Rev. Geophys.*, **42**(3), RG3001, doi:10.1029/2003RG000139.

Chelton, D. B. and R. E. Davis. 1982. "Monthly mean sea-level variability along the west coast of North America." *J. Phys. Ocean.*, 12, 757–784.

Collins, W. D., and coauthors. 2006a. "The Community Climate System Model version 3 (CCSM3)." *J. Climate*, **19**, 2122–2143.

Collins, W. D., and coauthors. 2006b. "The formulation and atmospheric simulation of the Community Atmosphere Model version 3 (CAM3)." *J. Climate*, **19**, 2144–2161.

Flick, R. E. 1998. "Comparison of California tides, storm surges, and mean sea level during the El Niño winters of 1982–83 and 1997–98." *Shore & Beach*, **66**(3), 7–11.

Flick, R. E., J. F. Murray, and L. C. Ewing. 2003. "Trends in United States tidal datum statistics and tide range." *J. Waterway, Port, Coastal and Ocean Eng.*, **129**(4), 155–164.

Gemmrich J., B. Thomas, and R. Bouchard. 2011. "Observational changes and trends in northeast Pacific wave records." *Geophys. Res. Lett.*, **38**, doi:10.1029/2011GL049518.

Graham, N. E. 1993. "Decadal-scale climate variability in the tropical and North Pacific during the 1970's and 1980's: Observations and model results." *Clim. Dyn.*, **10**, 135–162.

Graham, N. E. (Scripps Institution of Oceanography) 2005. *Coastal Impacts of North Pacific Winter Wave Climate Variability: The Southern California Bight and the Gulf of the Farallones*. For the California Energy Commission. PIER, Energy-Related Environmental Research, CEC-500-2005-018.

Heberger, M., H. Cooley, P. Herrera, P. H. Gleick, and E. Moore. 2009. *The Impacts of Sea Level Rise on the California Coast*. California Energy Commission. CEC-500-2009-024-F. 101 pp. http://www.pacinst.org/reports/sea_level_rise/report.pdf.

Hines, W. H., and D. C. Montgomery. 1980. *Probability and Statistics in Engineering and Management Science*. John Wiley & Sons, Inc., New York, 634pp.

Intergovernmental Panel on Climate Change. 2007. *Climate Change 2007: The Physical Science Basis*. Solomon, S. et al., Eds. Cambridge Univ. Press, Cambridge, UK, and New York.

Kalnay, E., and co-authors. 1996. The NCEP/NCAR 40-year reanalysis project. *Bull. Am. Meteorol. Soc.* 77(3): 437–471, doi:10.1175/1520-0477 (1996)077<0437:TNYRP>2.0.CO;2.

Kiehl, J. T., C. A. Shields, J. J. Hack, and W. D. Collins. 2006. "The climate sensitivity of the Community Climate System Model version 3 (CCSM3)." *J. Climate*, **19**, 2584–2596.

Kvamstø, N. G., Y. Song, I. A. Seierstad, A. Sorteberg and D. B. Stephenson. 2008. "Clustering of cyclones in the ARPEGE general circulation model." *Tellus A*, **60**, 547–556.

Legutke, S., and E. Maier-Reimer. 1999. *Climatology of the HOPE-G Global Ocean General Circulation Model, Technical Report, No. 21*. German Climate Computer Centre (DKRZ), Hamburg, 90 pp.

Liu, W. T., K. B. Katsaros, and J. A. Businger. 1979. "Bulk parameterization of air-sea exchange of heat and water vapor including the molecular constraints of the interface." *J. Atmos. Sci*., **36**, 1722–1735.

Lu, J., G. A. Vecchi, and T. Reichler. 2007. "Expansion of Hadley cell under global warming." *Geophys. Res. Lett*., **34**, L06805, doi:10.1029/2006GL028443.

Mantua, N. J. 2011. "The Pacific Decadal Oscillation (PDO)." Joint Institute for the Study of the Atmosphere and Ocean. http://jisao.washington.edu/pdo/.

Mantua, N. J., S. R. Hare, Y. Zhang, J. M. Wallace, and R. C. Francis. 1997. A Pacific interdecadal climate oscillation with impact on salmon production." *Bull. Am. Met. Soc*., **78**, 1069–1079.

Mendez, F. J., M. Menendez, A. Luceno, and I. J. Losada. 2007. "Analyzing monthly extreme sea levels with a time-dependent GEV model." *J. Atmos. Ocean. Tech*., **24**, doi: 10.1175/JTECH2009.1.

Merrifield, M. A. 2011. "A shift in western tropical Pacific sea level trends during the 1990s." *J. Clim*., **24**(15), 4126–4138.

Miller, A. J., D. R. Cayan, T. P. Barnett, N. E. Graham and J. M. Oberhuber. 1994. "The 1976-77 climate regime shift of the Pacific Ocean." *Oceanography*, **7**, 21–26.

O'Reilly, W. C., and R. T. Guza. 1991. "A comparison of spectral refraction and refraction-diffraction wave propagation models." *J. Waterway, Port, Coast. Ocean Eng.* 117(3): 199–215.

O'Reilly, W. C., and R. T. Guza. 1993. "A Comparison of Two Spectral Wave Models in the Southern California Bight." *Coastal Engineering* 19: 263–82.

Pugh, D. T., and J. M. Vassie. 1980. "Applications of the joint probability method for extreme sea level computations." *Proc. Inst. Civil Eng.* (Great Britain), **9**, 361–372.

Shepard, F. P. ed. 1963. *Submarine Geology*. Harper and Row, New York, 557 pp.

Stendel, M., and E. Roeckner. 1998. *Impacts of horizontal resolution on simulated climate statistics in ECHAM4. Report no. 253*, Max-Planck-Institut für Meteorologie, Bundesstr 55, Hamburg, 55pp.

Stockdon, H. F., R. A. Holman, P. A. Howd, and A. H. Sallenger. 2006. "Empirical parameterization of setup, swash, and runup." *Coastal Eng.*, **53**, 573–588.

Storlazzi, C. D. and G. B. Griggs. 2000. "Influence of El Niño-Southern Oscillation (ENSO) events on the evolution of central California's shoreline." *GSA Bulletin*, **112**(2), 236–249.

Storlazzi, C. D., C. M. Willis, and G. B. Griggs. 2000. "Comparative impacts of the 1982–83 and 1997–98 El Niño winters on the central California coast." *J. Coastal Res.*, **16**(4), 1022–1036.

Ruggiero, P., P. D. Komar, and J. C. Allan. 2010. "Increasing wave heights and extreme value projections: The wave climate of the U.S. Pacific Northwest." *Coastal Eng.*, **57**, 539–552.

Taboada, G., and R. Anadoin. 2010. "Critique of the methods used to project global sea-level rise from global temperature." *Proc. Nat. Acad. Sci.*, **107**(29), doi: 10.1073.pnas.0914942107.

Timmermann, A., S. McGregor, and F-F. Jin. 2010. Wind effects on past and future regional sea level trends in the southern Indo-Pacific." *J. Clim.*, **23**, 4429–4437.

Tolman, H. L. 1999. *User manual and system documentation of WAVEWATCH III, version 1.18*. U.S. Dept. of Commerce, NOAA, NWS, NCEP, Ocean Modeling Branch Contribution 166, 4700 Silver Hill Road, Mail Stop 9910, Washington, D.C. 20233–9910, 112pp.

Vermeer, M., and S. Rahmstorf. 2009. "Global sea level linked to global temperature." *Proc. Natl. Acad. Sci.*, **106**, 21527–21532.

# Glossary

| | |
|---|---|
| CC | central coast |
| CCSM3 | Community Climate System Model |
| CDIP | California Data Information Program |
| CNRM | Centre National de Recherches Meteorologiques |
| CPDF | cumulative probability density function |
| CRE | Crescent City |
| EH4 | Max Planck Institute for Meteorology EH4 model |
| ENSO | El Nino southern oscillation |
| EOF | empirical orthogonal function |
| GCM | global climate model |
| GHG | greenhouse gas |
| Hs | significant wave height |
| IPCC | Intergovernmental Panel on Climate Change |
| MPI | Max Planck Institute for Meteorology |
| MOP | monitoring and prediction |
| MSL | mean sea level |
| NC | northern coast |
| NCAR | National Center for Atmospheric Research |
| NCEP | National Centers for Environmental Prediction |
| NOAA | National Oceanic and Atmospheric Administration |
| PDO | Pacific decadal oscillation |
| PDF | probability density function |
| PIER | Public Interest Energy Research |
| RSL | relative sea level |
| SC | southern coast |
| SST | sea surface temperature |
| std | standard deviation |

| | |
|---|---|
| SFO | San Francisco |
| SIO | La Jolla |
| SLH | sea level height |
| SLP | sea level pressure |
| SML | San Miguel |
| SPAWAR | Space and Naval Warfare Systems Command |
| SWL | still water level |
| Tp | peak wave period |
| VR | Vermeer and Rahmstorf |
| WW3 | WAVEWATCH III model |

# Appendix A

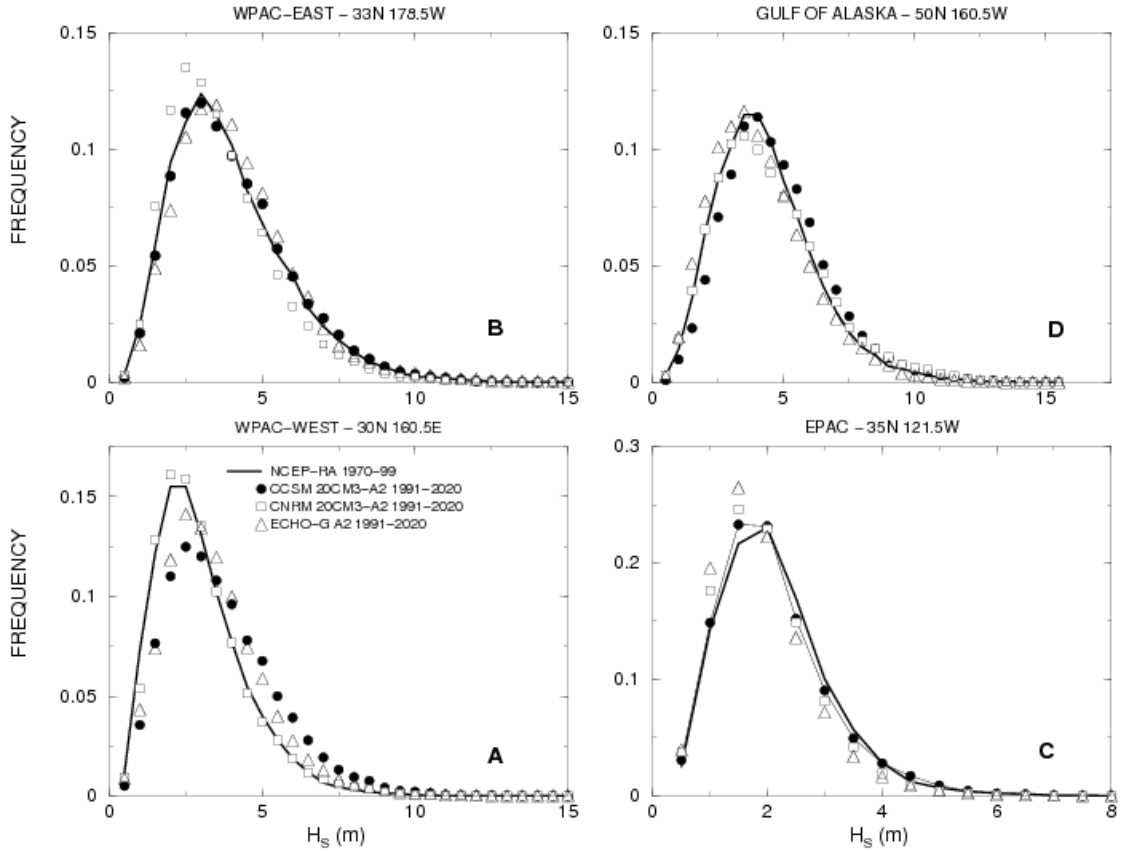


**Figure A1**. Frequency distributions of $H_{99}$ for NCEP-RA (1970–99; solid line), and combined 20CM3 and A2 results for 1991–2020 for CCSM (closed circles), CNRM (open squares) and EH4 (open triangles; note: figure legend incorrectly reads ECHO-G).